Article

Generalized three-dimensional lattice Boltzmann color-gradient method for immiscible two-phase pore-scale imbibition and drainage in porous media

LECLAIRE, Sébastien, *et al*.

Abstract

This article presents a three-dimensional numerical framework for the simulation of fluid-fluid immiscible compounds in complex geometries, based on the multiple-relaxation-time lattice Boltzmann method to model the fluid dynamics and the color-gradient approach to model multicomponent flow interaction. New lattice weights for the lattices D3Q15, D3Q19, and D3Q27 that improve the Galilean invariance of the color-gradient model as well as for modeling the interfacial tension are derived and provided in the Appendix. The presented method proposes in particular an approach to model the interaction between the fluid compound and the solid, and to maintain a precise contact angle between the two-component interface and the wall. Contrarily to previous approaches proposed in the literature, this method yields accurate solutions even in complex geometries and does not suffer from numerical artifacts like nonphysical mass transfer along the solid wall, which is crucial for modeling imbibition-type problems. The article also proposes an approach to model inflow and outflow boundaries with the color-gradient method by generalizing [...]

Reference

LECLAIRE, Sébastien, *et al*. Generalized three-dimensional lattice Boltzmann color-gradient method for immiscible two-phase pore-scale imbibition and drainage in porous media. *Physical Review. E*, 2017, vol. 95, no. 3, p. 033306

DOI : 10.1103/PhysRevE.95.033306

Generalized three-dimensional lattice Boltzmann color-gradient method for immiscible two-phase pore-scale imbibition and drainage in porous media

Sébastien Leclaire*
Department of Computer Science, University of Geneva, 7 route de Drize, 1227 Carouge, Switzerland and Department of Chemical Engineering, Polytechnique Montréal, 2500, chemin de Polytechnique, Montreal, H3T 1J4, Canada

Andrea Parmigiani
Department of Earth Sciences, Institute of Geochemistry and Petrology, ETH Zurich, Clausiusstrasse 25, 8092 Zürich, Switzerland

Orestis Malaspinas and Bastien Chopard
Department of Computer Science, University of Geneva, 7 route de Drize, 1227 Carouge, Switzerland

Jonas Latt
Department of Computer Science, University of Geneva, 7 route de Drize, 1227 Carouge, Switzerland and FlowKit Sàrl, Route d'Oron 2, 1010 Lausanne, Switzerland

(Received 21 October 2016; revised manuscript received 19 December 2016; published 14 March 2017)

This article presents a three-dimensional numerical framework for the simulation of fluid-fluid immiscible compounds in complex geometries, based on the multiple-relaxation-time lattice Boltzmann method to model the fluid dynamics and the color-gradient approach to model multicomponent flow interaction. New lattice weights for the lattices D3Q15, D3Q19, and D3Q27 that improve the Galilean invariance of the color-gradient model as well as for modeling the interfacial tension are derived and provided in the Appendix. The presented method proposes in particular an approach to model the interaction between the fluid compound and the solid, and to maintain a precise contact angle between the two-component interface and the wall. Contrarily to previous approaches proposed in the literature, this method yields accurate solutions even in complex geometries and does not suffer from numerical artifacts like nonphysical mass transfer along the solid wall, which is crucial for modeling imbibition-type problems. The article also proposes an approach to model inflow and outflow boundaries with the color-gradient method by generalizing the regularized boundary conditions. The numerical framework is first validated for three-dimensional (3D) stationary state (Jurin's law) and time-dependent (Washburn's law and capillary waves) problems. Then, the usefulness of the method for practical problems of pore-scale flow imbibition and drainage in porous media is demonstrated. Through the simulation of nonwetting displacement in two-dimensional random porous media networks, we show that the model properly reproduces three main invasion regimes (stable displacement, capillary fingering, and viscous fingering) as well as the saturating zone transition between these regimes. Finally, the ability to simulate immiscible two-component flow imbibition and drainage is validated, with excellent results, by numerical simulations in a Berea sandstone, a frequently used benchmark case used in this field, using a complex geometry that originates from a 3D scan of a porous sandstone. The methods presented in this article were implemented in the open-source PALABOS library, a general C++ matrix-based library well adapted for massive fluid flow parallel computation.

DOI: 10.1103/PhysRevE.95.033306

I. INTRODUCTION

Multiphase fluid flows in porous media finds its application in several environmental and industrial fields, such as dense, nonaqueous phase liquid (DNAPL) soils decontamination [1], CO2 storage in natural porous reservoirs [2], enhanced oil recovery [3], and migration of volcanic gas in evolved magmatic systems [4,5].

Although the pore-scale physics underlying immiscible multiphase fluid transport in porous media is essentially well understood, several recent contributions still explore and highlight interesting findings at this fundamental scale [6–8]. These advances contribute in important ways to filling the gaps of knowledge connecting the macroscopic Darcy scale to pore-scale models.

In this respect, the development and improvement of numerical tools capable of dealing with multiphase pore-scale processes powerfully contribute to this field. On the one hand, numerical simulation emerges as a flexible tool for engineering applications, and allows us for example to determine permeability curves for a given media [9]. On the other hand, simulation is a highly valuable tool for fundamental research in the field of multiphase fluid flows [10,11].

Popular methods for multiphase flow simulations include the volume of fluid [12] and level set [13] methods. More recently, the lattice Boltzmann technique, that belongs to the class of phase field methods, has shown its potential in the field of pore-scale multiphase fluid flow simulation [14].

*sebastien.leclaire@polymtl.ca

Historically, there exist three major classes of multiphase lattice Boltzmann methods:

(1) the color-gradient model (CGM) from Gunstensen and Rothman [15];

(2) the pseudopotential model from Shan and Chen [16]; and

(3) the free-energy model from Swift *et al.* [17].

The book of Huang *et al.* [18] offers an introduction to this field, and also includes other types of multiphase lattice Boltzmann methods. Liu *et al.* [19] review the multiphase lattice Boltzmann methods specifically in view of their application to porous media. For the interested reader, various numerical benchmarks are available that compare various multiphase lattice Boltzmann methods to each other, in Refs. [19–22]. A more general overview of the lattice Boltzmann methods can be found in Refs. [23–25]. It should also be noted that lattice Boltzmann methods for porous media flows were initially proposed in Refs. [26,27].

Because of the simplicity of its underlying algorithm and its theoretical relationship to microscopic physical phenomena, the Shan-Chen method [16] is still the most popular LB multiphase approach. Especially the multicomponent Shan-Chen model using two particle distribution functions is widely cited in the literature. However, in its traditional formulation this model is limited to the investigation of capillary regimes, where both density and viscosity differences between fluid are negligible or very limited [28,29]. With the help of recent improvements, the pseudopotential method can potentially be extended to high density and viscosity ratios [30–33].

The oldest lattice Boltzmann (LB) multiphase model, the CGM, has been improved in many different ways since it was published in 1992. Among the most popular three-dimensional versions available in the literature, we mention the model proposed by Tölke *et al.* [34], the one by Liu *et al.* [35], and the model by Li *et al.* [36]. While these models overcome numerous deficiencies of the original CGM, they still suffer from numerical artifacts. For example, they lack Galilean invariance [37] to a certain extent and appear to be physically inaccurate in multiphase flows with variable density ratios. In practice, this leads to a violation of the multiphase interface momentum jump condition (in the case of a momentum-based scheme) or velocity continuity [38] (in the case of a velocity-based scheme). Following Ref. [37], Leclaire *et al.* [39] improved the Galilean invariance of the CGM by proposing an enhanced version of the equilibrium distributions. Although not a CGM, the three-dimensional cascaded lattice Boltzmann model of Lycett-Brown *et al.* [40] further improves the Galilean invariance and scheme stability. However, the cascaded collision is not simple to work with, as the postcollision distributions are provided through quite complex expressions. This makes it difficult to incorporate new physics into this model.

One goal of the present paper is to propose a generalized three-dimensional two-phase lattice Boltzmann model which overcomes weaknesses of past models and is physically sound in a given range of parameters. It is based on the original three-dimensional CGM of Gunstensen and Rothman [15], but offers many additional improvements. More precisely, the model is an extension of the more recent two-dimensional model developed by Leclaire *et al.* [41]. We propose a given generalization to the three-dimensional lattices D3Q15, D3Q19, and D3Q27 of the enhanced equilibrium distribution functions [39], the multiple-relaxation-time (MRT) collision operator [42], and perturbation operator [43]. The model is built for the purpose of simulating important viscosity and density ratios between the immiscible phases, while respecting Galilean invariance with limited, but sufficient accuracy. In order to deal with Galilean invariance, the CGM proposed here uses the same technique as the one suggested for the free-energy method in Refs. [37,39]. The proposed CGM is adequate for the simulation of "immiscible multiphase" or "immiscible multicomponent" fluids. We use an isothermal equation of state, and it should be pointed out that as a consequence, the model is unable to reproduce multiphase scenarios with a change of phase. Such scenarios are, however, outside the scope of the present article. We emphasize that an isothermal equation of state is satisfactory for a large range of fully immiscible fluid flow situations. In this sense, the proposed CGM can be opposed to free-energy methods which usually seek to simulate phase-change and thus adopt a thermodynamically consistent pressure tensor.

The kinematic viscosity ratio in the CGM can be very large, reaching values of up to 1000 (see Ref. [19]). In particular, the kinematic viscosity ratio can be much larger than in the free-energy method, where it is restricted to values around 8 (see Ref. [19]). This makes the CGM a better choice than the free-energy method when it comes to simulate immiscible multicomponent fluids, where large differences of viscosity between the two fluids can occur. The scheme is mass and momentum conservative. It does not require the resolution of a Poisson equation at each time step and is therefore efficient and amenable to massive parallelization. The model does suffer from a certain amount of spurious currents, but these are easily controlled through a lattice refinement approach [44]. In the CGM, the numerical interface thickness (in lattice units), is constant in width in a simulation and controlled by a unique parameter. In contrast with the pseudopotential model, the CGM does therefore not suffer from interfaces that diffuse during the time evolution of the simulation. Furthermore, the numerical interface automatically converges toward a zero-width physical interface thickness with lattice refinement. We underline that the finite width of the fluid-fluid interface in the multicomponent lattice Boltzmann method introduces unphysical scales [45]. One approach to improve this issue is to use low-order interpolations near the fluid-fluid interface, and introduce boundary conditions that are discontinuous for some of the hydrodynamic variables, as described by Spencer *et al.* [45]. Our choice of the MRT collision operator, similar to the one proposed by Premnath and Abraham [46], leads to a model that is numerically very stable, yet much easier to implement than the cascaded LBM scheme of Ref. [40]. One of the most useful features of the model is that all physical and numerical parameters can be chosen independently: the interface thickness does for example not depend on the interfacial tension, as it does in a pseudopotential model. This makes the CGM very flexible and easy to use. One potential drawback of the CGM is that the collision is not completely local, as it requires nearest-neighbors information for the computation of the gradients. However, these added tasks add only little to the overall weight of interprocess

communication, as compared to the influence of the standard LBM streaming process. As a more severe restriction, we point out that while the CGM can simulate high density ratios in simple test cases, in complex setups it appears to be impractical to simulate density ratios larger than approximately 20, as this would require very small time steps and consequently long simulation times. While it is still possible to simulate a high density ratio with the CGM, it is clear that it still remains a real challenge [42,47]. We believe that current state-of-the-art CGMs are mostly suited for simulating liquid-liquid interfaces in immiscible, incompressible, and isothermal Newtonian multiphase flows [41], and in a limited sense for liquid-gas interfaces at very low Reynolds numbers.

Another interesting method for dealing with multicomponent fluids is the one proposed by Lishchuk *et al.* [48]. The interfacial physics is generated by adding a "hydrostatic" immersed boundary force alongside a measured interfacial curvature. This is different from the present CGM, which adopts the approach of Reis and Phillips [43], applying an immersed boundary force vector (divergence of a stress perturbation) at the interface of the fluid. At low Reynolds number, the first approach reduces the spurious currents more efficiently than the second approach. However, the correction to the fluid momentum in Lishchuk *et al.* [48] requires the evaluation of the interface curvature. This leads to an additional, non-negligible computational overhead, since second-order derivatives need to be computed at each time step. It is, furthermore, unclear how the approach by Lishchuk *et al.* [48] could be applied to multiple immiscible fluids.

In lieu of a full review of the state of art for the CGM, we now discuss below a few recent CGM publications applied to porous media applications.

Li *et al.* [36] demonstrate that the CGM is well suited for an implementation on graphical processing units (GPUs). They investigate flows in porous media and find that the residual oil saturation is affected by both interfacial tension and solid wettability. This article does, however, not provide any theoretical validation beyond a simple validation of the Laplace law. Other articles show that this type of CGM may not be able to solve flows adequately with nonunit density ratio in complex test cases and require special adjustment to improve their accuracy [39,49].

Gunde *et al.* [50] compute relative permeability curves and obtain qualitative insights regarding the physics of water flooding in naturally fractured reservoirs, using the original two-color model from Gunstensen *et al.* [51] with the recoloring algorithm from Latva-Kokko and Rothman [52]. This work is purely bidimensional. Furthermore, it does not make use of recent improvements to the algorithm, like the use of isotropic color gradients [53], which substantially improve its accuracy.

Huang *et al.* [54] draw a complete phase diagram of the dynamic viscosity ratio against the capillary number [55] using the lattice Boltzmann method. This is an important step for the understanding of multiphase flows in porous media. This work is, however, also purely bidimensional. Furthermore, as shown in the recent literature, the numerical method used in Huang *et al.* must be treated with special care. Indeed, Huang *et al.* use a technique for modeling contact angle based on imposing fictitious densities on the walls, which is known to lead to a severe lack of accuracy due to a nonphysical fluid transfer along the solid wall [44]. This numerical deficiency is not visible in the numerical experiments of Huang *et al.*, because in these cases, the periodic boundary condition guarantees a balance of artificial mass flow along the walls. This is, however, not the case in more general, nonperiodic problems. As an example, the present article shows, in the Berea sandstone benchmark, that the fictitious-density approach to contact angles is insufficient for the simulation of multicomponent imbibition flow through porous media.

Jiang *et al.* [56] investigate multiphase flows into a Berea sandstone using a three-dimensional CGM implemented on GPUs. They found that for a flow driven by a pressure gradient, the physics of the fluid displacement can be described by three distinct regimes, which highly depend on the interfacial tension. As the interfacial tension force is increasing, the authors observe viscous fingering to capillary fingering up to a situation where the invading fluid failed to break through. Indeed, that, if the interfacial tension force is high enough, the overall pressure gradient might not be high enough to compensate the Laplace pressure jump [57]. As further limitations, we point out that Jiang *et al.* use the fictitious density approach for contact angles which, as pointed out above, is limited.

Liu *et al.* [58] studied dual-permeability porous media and compared them to randomly heterogeneous media. They found, among other things, that the transition from capillary fingering to viscous fingering appears at higher capillary number in randomly heterogeneous media. Washburn's law was validated for cases in which both fluid viscosities are non-negligible, which is an important validation of the CGM. Their investigation is, however, also limited to bidimensional flows and to unit density ratio. Furthermore, just like in previous studies, the standard [44] and potentially inaccurate fictitious-density boundary condition was used in this work. In a more recent work and using the same model, Liu *et al.* [59] studied multiphase flows in homogeneous pore networks and compared them to randomly heterogeneous pore networks. They found, similarly as Lenormand *et al.* [55], three different displacement patterns: stable displacement, capillary fingering, and viscous fingering.

Tsuji *et al.* [60] studied two-phase flow behaviors in three-dimensional (3D) natural rocks, and classified the flow patterns according to the phase diagram by Ref. [55]. They demonstrated that a digital rock approach is suitable for revealing pore-scale phenomena. Their study is based on the CGM of Tölke *et al.* [61]. Again, the limited density ratio between the fluid components seems to be the main limitation of their approach. Indeed, the literature suggests that the Tölke *et al.* model fails to model variable density ratios in simple benchmark cases like Couette flows [62].

It is our opinion that all the methods and techniques discussed above clearly illustrate the potential of the CGM when it comes to modeling immiscible fluid flows at the pore-scale level. The CGM can therefore be considered a mature tool for both industry and academia for the characterization of porous media. However, all the CGM methods described above still suffer from some deficiencies, as they may lack Galilean invariance to a certain extent and therefore may be inaccurate for simulating flow with density ratio in many practical situations [37,39,41,49,62]. Consequently, they can

only simulate multicomponent flow through porous media with a more limited ratio of dynamic viscosity. All these models also generally use the fictitious-density boundary conditions in situations of wetting fluids. Because of nonphysical mass transfers, these wetting boundary conditions are, however, only suitable when the invading fluid is nonwetting [44]. Consequently, there is a need for a fully three-dimensional CGM with more accurate wetting boundary condition, able to simulate density ratios that are large enough for describing a vast range of fluid-fluid compounds.

The present article addresses the mentioned drawbacks of previously used models and proposes several improvements. First, we include a more robust three-dimensional wetting boundary condition. While we have previously shown that this type of CGM can simulate flows with variable density ratios [39,41], we focus in the present article on validating our wetting boundary condition against (1) Jurin's law [63,64] and (2) Washburn's law [65]. The GCM fluid-fluid interaction is also further validated against (3) three-dimensional capillary waves [66] for variable density and viscosity ratios. After these validations, we test the quality of our model for multiphase pore-scale applications, studying first two-phase fluid flows in two-dimensional random porous media networks. In this case, we show that the model is capable of reproducing the three major invasion regimes of nonwetting displacement in porous media as well as the saturation zone transition (stable displacement, capillary fingering, and viscous fingering) as described by Lenormand *et al.* [55]. In order to be able to simulate these cases with the CGM, and with variable density ratios, we developed different density and velocity boundary condition for the CGM. It is a generalization of the LB regularized density and velocity boundary condition proposed by Ref. [67]. We finally conclude our work with an application of our method to concrete 3D application scenarios, by running imbibition and drainage experiments through 3D Berea sandstone digital images. In this context, we highlight the importance of using our wetting boundary condition, which we compare to the traditional one, using fictitious wall densities. We provide open-source implementations of the CGM described in this article to the scientific community through the PALABOS library [68]. These extensions are theoretically valid for all lattices D2Q9, D3Q15, D3Q19, and D3Q27, although for the CGM, only the code for the three-dimensional lattices is currently available.

II. LATTICE BOLTZMANN COLOR-GRADIENT METHOD

The contribution of the present article to the color-gradient method concerns the three-dimensional generalization as well as a different three-dimensional wetting boundary condition, which is inspired from a previous two-dimensional wetting boundary condition [44]. We also generalized the single-phase regularized density and velocity lattice Boltzmann boundary conditions [67] to LB models in which the zero-velocity population has a variable weight. This generalization is necessary for the multiphase CGM for nonunity density ratios, because in these cases the weight of zero-velocity population is used to implement density differences.

The proposed two-phase model is described in a general way, for any given DmQn lattice. All the necessary notations, constants, weights, stencils, connectivity vectors, indexes, and matrices are supplied in the Appendix. We describe the model in the so-called lattice units, which are for example introduced in Ref. [69].

For each fluid, a set of colored distribution functions $N_i^k(\mathbf{x},t)$ is described on a DmQn lattice $\mathbf{X}_L$, with lattice connectivity vectors $\mathbf{c}_i$ as provided in the Appendix. The distribution functions are labeled with a superscript k, which is equal to r for a red fluid and b for a blue fluid. The subscript index i is related to the velocity space discretization. The color-blind distribution function is denoted as $N_i(\mathbf{x},t) = N_i^r(\mathbf{x},t) + N_i^b(\mathbf{x},t)$.

The various lattice sites are regrouped into two disjoint sets $\mathbf{X}_F$ and $\mathbf{X}_S$, representing fluid sites $\mathbf{X}_F$ and solid sites $\mathbf{X}_S$ respectively. The sites $\mathbf{X}_E \subset \mathbf{X}_F$ are associated with the external boundary conditions, such as density or velocity boundary conditions. The set $\mathbf{X}_W \subset \mathbf{X}_F$ corresponds to the fluid sites that have at least one solid neighbor, situated in $\mathbf{X}_S$.

The main loop of the proposed evolution algorithm from time t to $t+1$ is summarized as follows:

(1) external boundary condition: $N_i^k(\mathbf{x},t_*)=(\Omega)^{(0)}(N_i^k(\mathbf{x},t)),\forall k, \forall i$ and $\forall \mathbf{x} \in \mathbf{X}_E$;

(2) single-phase collision: $|N(\mathbf{x},t_{**})\rangle = (\Omega)^{(1)}(|N(\mathbf{x},t_*)\rangle)$, $\forall \mathbf{x} \in \mathbf{X}_F$;

(3) wetting boundary condition: modification of the normal vector to the fluid interface near the solid boundary $\forall \mathbf{x} \in \mathbf{X}_W$;

(4) multiphase collision (perturbation): $N_i(\mathbf{x},t_{***}) = (\Omega)^{(2)}(N_i(\mathbf{x},t_{**}))$, $\forall i$ and $\forall \mathbf{x} \in \mathbf{X}_F$;

(5) multiphase collision (recoloring): $N_i^k(\mathbf{x},t_{****}) = (\Omega)^{(3)}(N_i(\mathbf{x},t_{***}))$, $\forall k, \forall i$ and $\forall \mathbf{x} \in \mathbf{X}_F$;

(6) full-way bounce back boundary conditions [70]: $N_i^k(\mathbf{x},t_{*****}) = N_{\mathrm{opp}(i)}^k(\mathbf{x},t_{****})$, $\forall k, \forall i$ and $\forall \mathbf{x} \in \mathbf{X}_S$;

(7) streaming operator: $N_i^k(\mathbf{x}+\mathbf{c}_i,t+1) = N_i^k(\mathbf{x},t_{*****})$, $\forall k, \forall i$ and $\forall \mathbf{x} \in \mathbf{X}_L$ where the symbol $|.\rangle$ denotes the bra Dirac notation for an expansion in velocity space, along the indexes i. The term $\mathrm{opp}(i)$ denotes the opposite orientation.

A. Single-phase collision operator

The first operator $(\Omega)^{(1)}$, is based on the standard MRT operator of the single-phase LB model [71]. The moments are relaxed towards a local equilibrium, in which $\mathbf{K}$ denotes a diagonal matrix of relaxation coefficients, and $\mathbf{M}$ is the matrix that shifts the domain from a distribution space to a moment space,

$$(\Omega)^{(1)}(|N\rangle) = |N\rangle - \mathbf{M}^{-1}\mathbf{K}\mathbf{M}(|N\rangle - |N^{(e)}\rangle) + |\Delta N\rangle. \quad (1)$$

The density of the fluid k is given by the first moment of the distribution functions:

$$\rho_k = \sum_i N_i^k. \quad (2)$$

The total fluid density is given by $\rho = \sum_k \rho_k$, while the total momentum is defined as the second moment of the color-blind distribution functions:

$$\rho\mathbf{u} = \sum_i N_i \mathbf{c}_i, \quad (3)$$

where $\mathbf{u}$ is the velocity of the color-blind distribution functions. Based on Refs. [37,39], the general form of the DmQn

equilibrium functions is defined by

$$N_i^{(e)}(\rho,\mathbf{u}) = \overline{\nu}[\psi_i(\mathbf{u}\cdot\nabla\rho)+\xi_i(\mathbf{G}:\mathbf{c}_i\otimes\mathbf{c}_i)] + \rho\left[\phi_i+\varphi_i\overline{\alpha}+W_i\left(3\mathbf{c}_i\cdot\mathbf{u}+\tfrac{9}{2}(\mathbf{c}_i\cdot\mathbf{u})^2-\tfrac{3}{2}\mathbf{u}\cdot\mathbf{u}\right)\right], \tag{4}$$

where $\otimes$ is the tensor product, the symbol ":" stands for the tensor contraction, and the superscript (e) denotes equilibrium. The tensor $\mathbf{G}$ is defined by

$$\mathbf{G} = (\mathbf{u}\otimes\nabla\rho)+(\mathbf{u}\otimes\nabla\rho)^{\intercal}, \tag{5}$$

where the superscript $\intercal$ is the transpose operator. The weights ψ_i, ξ_i, ϕ_i, φ_i, and W_i are lattice dependent and are given in Tables II–V in the Appendix. The methodology to derive these weights is also described in the Appendix.

The term $|\Delta N\rangle$ in Eq. (1) is a density distribution function modification designed to add external forces. In this research, this term is solely used to change momentum so that the fluid acceleration such as gravity is taken into account:

$$|\Delta N\rangle = \mathbf{M}^{-1}|\Delta m\rangle, \tag{6}$$

where $|\Delta m\rangle$ is a vector with all components equal to zero except for the indexes corresponding to the momentum such that

$$\Delta m_{p_x} = \rho g_x, \tag{7}$$

$$\Delta m_{p_y} = \rho g_y, \tag{8}$$

$$\Delta m_{p_z} = \rho g_z, \tag{9}$$

where $\mathbf{g}=[g_x,g_y,g_z]$ is the gravity acceleration and the momentum indexes p_x, p_y, and p_z are lattice dependent and are given in Table VII.

As established in Ref. [72], the density ratio between the fluids γ must be taken into account as follows to obtain a stable interface:

$$\gamma = \frac{\rho_r^0}{\rho_b^0} = \frac{1-\alpha_b}{1-\alpha_r}, \tag{10}$$

where the superscript "0" over ρ_r^0 or ρ_b^0 indicates the initial value of the density at the beginning of the simulation.

In each homogeneous phase region, the pressure of the fluid k is

$$p_k = \rho_k\zeta(1-\alpha_k) = \rho_k\left(c_s^k\right)^2. \tag{11}$$

In the above expressions, only one α_k is a free parameter because of the constraint in Eq. (10). In general, we let the blue fluid be the least dense, and we set the value of $0<\alpha_b = W_0<1$ so that the relation $0<\alpha_b\leqslant\alpha_r<1$ is guaranteed to hold. This relation needs to be respected to avoid nonphysical negative pressure. Also, these parameters set the isothermal sound speed c_s^k in each fluid k. The weight ζ is also lattice dependent and is given in Table VI. The parameters $\overline{\alpha}$ in the equilibrium Eq. (4) is the arithmetic density weighted average:

$$\overline{\alpha} = \frac{\rho_r}{\rho_r+\rho_b}\alpha_r+\frac{\rho_b}{\rho_r+\rho_b}\alpha_b. \tag{12}$$

The MRT matrix $\mathbf{M}$ is lattice dependent and is given in Tables IX–XII for various lattices. These matrices are derived similarly as in Refs. [73–75]; the only difference here concerns the ordering indexes i of the velocity space which is different from these studies. It has been judged pertinent to reproduce them in the present article so that all the matrices and indexes are presented here with the same ordering of the lattice connectivity vectors. The diagonal matrix $\mathbf{K}$ is also lattice dependent and the diagonal coefficients $K_{\upsilon,\upsilon}$ are related to the viscosity of the fluids, so their values are set to the usual effective relaxation parameter ω_{eff}. The indexes υ are given in Table VIII for various lattices. The other diagonal coefficients are set to $\chi\omega_{\text{eff}}$. The constant factor $0<\chi\leqslant 1$ may improve the stability of the model. With $\chi=1$, the multiple-relaxation-time operator becomes a single-relaxation-time operator; lowering the value of χ may therefore make the model more stable [42]. However, lowering this value too much may affect accuracy.

The effective relaxation parameter ω_{eff} is defined so that the fluid viscosity is consistent with the macroscopic equations for a single-phase flow in the single-phase regions. When the viscosities of the fluids are different, an interpolation is applied to define the parameter ω_{eff} at the interface. If ν_k is the kinematic viscosity of the fluid k, we use the harmonic density weighted average to define the viscosity $\overline{\nu}$ at the interface between the fluids:

$$\frac{1}{\overline{\nu}} = \frac{\rho_r}{\rho_r+\rho_b}\frac{1}{\nu_r}+\frac{\rho_b}{\rho_r+\rho_b}\frac{1}{\nu_b}. \tag{13}$$

Note that other viscosity interpolation schemes are possible [62]. Then, the effective relaxation parameter is

$$\omega_{\text{eff}} = \frac{2}{6\overline{\nu}+1}. \tag{14}$$

B. Perturbation operator

The interfacial tension in the CGM is modeled by means of the perturbation operator [43,51]. It may take the following form:

$$(\Omega_i)^{(2)}(N_i) = N_i+\Delta N_i^{\text{pert}}, \tag{15}$$

where the perturbation term ΔN_i^{pert} is

$$\Delta N_i^{\text{pert}} = A|\mathbf{F}|\left[W_i\frac{(\mathbf{F}\cdot\mathbf{c}_i)^2}{|\mathbf{F}|^2}-B_i\right] \tag{16}$$

in which the color gradient $\mathbf{F}$ approximates the normal to the interface:

$$\mathbf{F} = \nabla\left(\frac{\rho_r-\rho_b}{\rho_r+\rho_b}\right) \tag{17}$$

and B_i are lattice dependent weights given in Tables II–V. Reis and Phillips [43] and Liu *et al.* [35] have shown that this operator complies within the macroscopic limit, with the capillary stress tensor present in the macroscopic equations for two-phase flows if the weights B_i are well chosen. The parameter A is space and time dependent and is chosen to fit the interfacial tension σ at the fluid interface:

$$A = \tfrac{9}{4}\omega_{\text{eff}}\sigma. \tag{18}$$

Although this operator generates the interfacial tension, it does not guarantee the fluid's immiscibility. To minimize mixing

and segregate the fluids, the recoloring operator $(\Omega_i^k)^{(3)}$ needs to be properly selected.

C. Recoloring operator

This operator is used to maximize the amount of fluid k at the interface that is sent to the fluid k region, while remaining consistent with the laws of conservation of mass and total momentum. The recoloring operator presented here is based on Refs. [52,76], and is as follows:

$$\left(\Omega_i^r\right)^{(3)}(N_i) = \frac{\rho_r}{\rho} N_i + \beta \frac{\rho_r \rho_b}{\rho^2} \cos(\vartheta_i) N_i^{(e)}(\rho, \mathbf{0}), \tag{19}$$

$$\left(\Omega_i^b\right)^{(3)}(N_i) = \frac{\rho_b}{\rho} N_i - \beta \frac{\rho_r \rho_b}{\rho^2} \cos(\vartheta_i) N_i^{(e)}(\rho, \mathbf{0}), \tag{20}$$

where $\beta = \beta^*(\Delta x/\Delta x^*)^\eta$ is a parameter controlling the thickness of the numerical interface [77]. The spacing Δx^* and Δx are physical spacing steps, not spacing steps in lattice units. The superscript "*" corresponds to a reference value, so that β^* and Δx^* are the values that would be used on a coarse lattice. The parameter η is linked to the rate at which the numerical interface thickness is reduced in the physical space with lattice refinement [77]. The angle ϑ_i corresponds to the one between the color gradient $\mathbf{F}$ and the lattice connectivity vector $\mathbf{c}_i$.

D. Single-phase regularized density and velocity boundary conditions with a variable zero velocity lattice weight

The modeling of isothermal multiphase immiscible flows with density ratios and with the color-gradient method requires us to adjust the zero velocity lattice weight α_k. In the common color-gradient algorithm, this weight is usually only linked with the isothermal speed of sound c_s^k. However, changing the zero velocity weight α_k results in changes of other underlying lattice weights required for the implementation of the single-phase regularized density and velocity boundary conditions. Proper care needs to be taken to model the expected physics of the regularized boundary conditions. We define the weights in a way similar to Nourgaliev *et al.* [78], where two lattice weights $\Upsilon_k^{(2)}$ and $\Upsilon_k^{(4)}$, which depend on the lattice geometry, need to be defined. The first weight $\Upsilon_k^{(2)}$ is the usual square of the color-gradient isothermal speed of sound:

$$\Upsilon_k^{(2)} = \left(c_s^k\right)^2. \tag{21}$$

The weight $\Upsilon_k^{(4)}$, on the other hand, is linked to the constitutive physics $\mathcal{M} = \lambda\rho$ [78]:

$$\Upsilon_k^{(4)} = \lambda \Upsilon_k^{(2)}, \tag{22}$$

where λ is a constitutive physics coefficient, related only to the fluid viscosity. This coefficient happens to have the value $\lambda = \frac{1}{3}$ for all lattice models D2Q9, D3Q15, D3Q19, and D3Q27 (see the Appendix). This is a subtle consideration that needs to be taken into account for the implementation of the single-phase regularized density and velocity boundary conditions with the color-gradient method. Indeed, usually in the single-phase lattice Boltzmann method $\alpha_k = W_0$ for all lattices D2Q9, D3Q15, D3Q19, and D3Q27, leading to $\Upsilon_k^{(2)} = (c_s^k)^2 = 1/3$ and $\Upsilon_k^{(4)} = (c_s^k)^4 = 1/9$. However, with a variable zero velocity weight $\alpha_k \neq W_0$, the weights are $\Upsilon_k^{(2)} = (c_s^k)^2 \neq 1/3$ and $\Upsilon_k^{(4)} \neq (c_s^k)^4$. This is the main difference accounted for in our extended single-phase regularized density and velocity boundary conditions, allowing the usage of the regularized boundary conditions with the color-gradient method with variable density ratios.

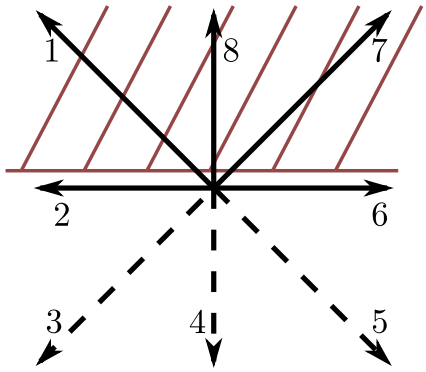

FIG. 1. A boundary node example for the D2Q9 lattice. The dashed arrows represent the unknown populations.

The rest of this section briefly presents the regularized boundary condition for the lattice Boltzmann method that takes into account a variable zero velocity weight α_k. For more details on this boundary condition, we refer the reader to Ref. [67]. For more information on boundary conditions in general in the lattice Boltzmann method, the interested reader is referred to Refs. [79–82].

In our algorithm, the regularized boundary conditions are implemented at steps (1) $\forall \mathbf{x} \in \mathbf{X}_E$. Therefore, on a boundary grid node some populations are unknown before the single-phase collision, since they are streamed "from outside" the computational domain, as depicted (for simplicity this example is done in two dimensions) in Fig. 1. Thus they have to be computed in an *ad hoc* manner. In this paper, the regularized boundary conditions are based on a reconstruction of populations with the help of their Chapman-Enskog expansion.

Note that we now omit the index "k" for the color of the fluid, as we assume that all boundary nodes are covered homogeneously by a single fluid component. However, the value of $\Upsilon^{(2)}$ and $\Upsilon^{(4)}$ at the boundary node still depends on the overall density ratio γ of the fluids.

The main idea is to reconstruct all the populations of the boundary node according to their Chapman-Enskog formulation:

$$N_i = N_i^{(0)}(\rho_{\mathrm{bc}}, \boldsymbol{u}_{\mathrm{bc}}) + N_i^{(1)}\left(\boldsymbol{P}_{\mathrm{bc}}^{(1)}\right), \tag{23}$$

where ρ_{bc}, $\boldsymbol{u}_{\mathrm{bc}}$, and $\boldsymbol{P}_{\mathrm{bc}}^{(1)}$ are the values of the density ρ, the velocity $\boldsymbol{u}$, and the deviatoric stress tensor $\boldsymbol{P}^{(1)}$ on the boundary node. The superscripts (0) and (1) denote quantities computed from the equilibrium and off-equilibrium distributions respectively.

We discuss two kinds of boundary conditions here:

(1) The velocity boundary conditions (or Dirichlet), where $\boldsymbol{u}_{\mathrm{bc}}$ is imposed. In this case, in order to be able to use Eq. (23), one must still compute ρ_{bc} and $\boldsymbol{P}_{\mathrm{bc}}^{(1)}$.

(2) The pressure $p_{\rm bc}$ (or density $\rho_{\rm bc} = p_{\rm bc}/c_s^2$) is imposed, as well as the velocity components tangential to the boundary (noted $u_\parallel$). In this case, in order to use Eq. (23) one must still compute $u_\perp$ (the component of the velocity normal to the boundary) and $\boldsymbol{P}^{(1)}_{\rm bc}$.

We first focus on the computation of $\rho_{\rm bc}$ or $u_\perp$, which are related through the equation presented in Ref. [83]:

$$\rho_{\rm bc} = \frac{1}{1+u_\perp}(2\rho_+ + \rho_0), \tag{24}$$

where $u_\perp = \boldsymbol{u}_{\rm bc}\cdot\boldsymbol{n}$ is the boundary velocity projected onto the boundary outward normal unit vector $\boldsymbol{n}$. The quantities ρ_0 and ρ_+ are defined as

$$\rho_0 = \sum_{i\in\{i|\boldsymbol{c}_i\cdot\boldsymbol{n}=0\}} N_i, \tag{25}$$

$$\rho_+ = \sum_{i\in\{i|\boldsymbol{c}_i\cdot\boldsymbol{n}>0\}} N_i. \tag{26}$$

At the leading order the off-equilibrium populations $N_i^{(1)}$ are related to the deviatoric stress through

$$N_i^{(1)} = \frac{W_i}{2\Upsilon^{(4)}}\boldsymbol{Q}_i : \boldsymbol{P}^{(1)}, \tag{27}$$

where $\boldsymbol{Q}_i = \boldsymbol{c}_i\boldsymbol{c}_i - \Upsilon^{(2)}\boldsymbol{I}$, with $\boldsymbol{I}$ is the identity matrix. In the usual regularized boundary condition (see Ref. [67]), the term $\Upsilon^{(4)}$ is replaced by c_s^4. The method proposed here is more general, as it takes into account possible variations of the zero velocity lattice weight.

Since $\boldsymbol{Q}_i = \boldsymbol{Q}_{{\rm opp}(i)}$ [where opp(i) labels the direction opposite to the direction pointed by $\boldsymbol{c}_i$] one can impose the following relation at leading order:

$$N_i^{(1)} = N_{{\rm opp}(i)}^{(1)}, \quad \forall i|\boldsymbol{c}_i\cdot\boldsymbol{n}<0. \tag{28}$$

Then

$$\boldsymbol{P}^{(1)} = \sum_i \boldsymbol{Q}_i N_i^{(1)} \tag{29}$$

and N_i can be reconstructed according to Eq. (23).

E. Wetting boundary condition

In this section, our methodology for imposing a wetting boundary condition is described in detail. The idea is based on the fact that, with this lattice Boltzmann method, a precise contact angle can be imposed by changing only $\mathbf{n}_c$, the unit normal to the fluid interface, near the boundary $\forall\mathbf{x}\in\mathbf{X}_W$. Equivalently, the contact angle is set by changing the current orientation of the color gradient $\mathbf{F} = |\mathbf{F}|\mathbf{n}_c$, so that its angle with the normal direction to the wall $\mathbf{n}_w$ is equal to the desired contact angle θ_c. This numerical procedure must be executed at each time step right before the implementation of the wetting boundary condition, which is right after the *a priori* approximation of the color gradient $\mathbf{F}$ that would be computed with finite differences, using only the currently known information from the bulk fluid lattice sites. Overall, this is a kind of Dirichlet boundary condition only for the orientation of the color gradient $\mathbf{F}$, because the norm of the color gradient $|\mathbf{F}|$ remains unchanged by the wetting boundary condition. To illustrate the basic concepts, let us first assume that an approximated direction to the wall normal $\mathbf{n}_w$ is known for each fluid site in $\mathbf{X}_W$. In other words, we take it for granted that $\mathbf{n}_c$ and $\mathbf{n}_w$ are *a priori* estimates at a given fluid site near the boundary, although the angle between them is not equal to θ_c. The goal of the wetting boundary condition is to change the orientation of $\mathbf{n}_c$ relative to $\mathbf{n}_w$ in order to achieve the correct contact angle θ_c between the two vectors. It will be explained later on how to compute the *a priori* approximation of the wall normal $\mathbf{n}_w$.

The first step of the algorithm is to find a new vector $\mathbf{v}_c$, that replaces the *a priori* estimation $\mathbf{n}_c$ and that, ideally, forms an angle θ_c with $\mathbf{n}_w$. For the new vector $\mathbf{v}_c$ to form a contact angle of θ_c with $\mathbf{n}_w$, it needs at least to respect the following equation:

$$f(\mathbf{v}_c) = \mathbf{v}_c\cdot\mathbf{n}_w - |\mathbf{v}_c|\cos(\theta_c) = 0. \tag{30}$$

This is a degenerate system with one equation and three unknowns, as each component of $\mathbf{v}_c$ corresponds to one unknown. Therefore, the set of solutions is infinitely large. More precisely, the solution set is described by the equation of a circle in three-dimensional space, the circle being generated by taking all vectors that form an angle θ_c with $\mathbf{n}_w$. Overall, it is a difficult problem to choose the most adequate solution in this set. Although the system is degenerate, it is still possible to use the numerical method of the secant to extract one particular solution without dealing with complex three-dimensional vector transformations and projections. As a function of the index n, the proposed recurrence relation for the secant method can be expressed as follows:

$$\mathbf{v}_c^{(0)} = \mathbf{n}_c, \tag{31}$$

$$\mathbf{v}_c^{(1)} = \mathbf{n}_c - \lambda(\mathbf{n}_c + \mathbf{n}_w), \tag{32}$$

$$\mathbf{v}_c^{(n)} = \frac{\mathbf{v}_c^{(n-2)} f\left(\mathbf{v}_c^{(n-1)}\right) - \mathbf{v}_c^{(n-1)} f\left(\mathbf{v}_c^{(n-2)}\right)}{f\left(\mathbf{v}_c^{(n-1)}\right) - f\left(\mathbf{v}_c^{(n-2)}\right)}. \tag{33}$$

In this case, the specific choice of the initial values $\mathbf{v}_c^{(0)}$ and $\mathbf{v}_c^{(1)}$ imposes a search direction for the proposed secant method. As a result, the solution $\mathbf{v}_c$ is situated in the plane spanned by $\mathbf{n}_c$ and $\mathbf{n}_w$. This is due to the fact that the secant method proposed here is based on linear vector combinations only, with base vectors $\mathbf{n}_c$ and $\mathbf{n}_w$. For simplicity, we used $\lambda = 1/2$, but other values of λ or even different initial conditions could potentially improve the numerical accuracy. However, finding a solution to Eq. (30) in the space spanned by $\mathbf{n}_c$ and $\mathbf{n}_w$ is a reasonable search hypothesis, as a solution in this plane is guaranteed to exist. Also, since $\mathbf{v}_c^{(0)} = \mathbf{n}_c$, the secant method computes a new vector $\mathbf{v}_c^{(n)}$, close to the color-gradient orientation $\mathbf{n}_c$, which is estimated from the bulk fluid lattice sites. Although this recurrence relation would in principle need to be carried out for many iterations to find an exact solution, we decide in our algorithm to always stop at $n = 2$ to avoid any unnecessary computational costs. Indeed, the lattice Boltzmann method itself is an explicit time-stepping scheme which is carried out at very small time steps. The angle of the fluid interface therefore changes only very little from one LBM time step to the next, leading to a good initial value for the iterations of the secant method. At the end of the algorithm to impose a wetting boundary condition, since the recurrence relation does

not guarantee the resulting vector to be of unit norm, the vector $\mathbf{v}_c^{(2)}$ is normalized before it replaces the current orientation of the color gradient $\mathbf{n}_c$. After this, the execution of the CGM's perturbation step takes place. Assuming that a prediction of the color gradient $\mathbf{F}$ and of the normal vector to the solid boundary $\mathbf{n}_w$ is available, this wetting boundary condition is fully local.

This proposed wetting boundary condition is similar to the one provided by Tölke *et al.* [84]. However, in their work, the authors end up with a nonlinear system with five equations and five unknowns. Their system is solved with a Newton-Raphson method which could end up being expensive in computational resources. Here, the final system has only one equation with three unknowns and is solved with the simpler secant method. It is clear that our approach is unusual because the system is degenerate, but still provides good results thanks to the chosen initial condition of the secant method. Indeed, as already mentioned above, the search for the numerical solution is restricted to the plane generated by $\mathbf{n}_c$ and $\mathbf{n}_w$, and also the solution is assumed to be close to $\mathbf{n}_c$. It is guaranteed that a numerical solution exists in that plane, and it is most likely to be very close to $\mathbf{n}_c$.

We would like to add a side note concerning the widely used standard wetting boundary condition [44]. The standard approach consists of imposing fictitious colored densities in the solid lattice sites in order to influence the orientation of the nonlocal gradients $\mathbf{F}$. It has been shown in a previous publication that this approach may lead to a nonphysical fluid flow in a thin layer along the solid boundary. This can spoil the numerical results [44]. But on top of this, since the contact angle is also not accurately captured with this approach, the fictitious colored densities must often be fine-tuned for every choice of simulated regime parameters. This is a time-consuming task, and even if a setting seems to work well for a given set of flow parameters and for a simple geometry, a more complex geometry would inevitably lead to additional inaccuracies, or even to results that completely deviate from any physically meaningful solution. The proposed wetting boundary condition is much more general in the sense that it automatically works for complex geometry and is independent of additional imposed parameters, e.g., density and viscosity ratios.

Estimation of $\mathbf{n}_w$ *near the solid boundary*

A pore matrix is frequently obtained by micro computed tomography imaging of rock samples [85]. These scans provide "gray" matrix while the LBM usually required a "binary" matrix to describe the fluid-solid boundary. Therefore, the true position of the fluid-solid interface is never exactly known and is only an approximation in the simulations. So for a three-dimensional fluid-solid matrix, it is overall very difficult to find accurately what is the true position and the orientation of the normal vector to the solid wall and to impose it into a simulation. Here, it is assumed that a binary fluid-solid matrix is already available and use a simple approach to estimate the position and the normal vector to the solid wall $\mathbf{n}_w$. In order to estimate $\mathbf{n}_w$ at the fluid lattice sites near the solid boundary, the three-dimensional solid matrix image is first smoothed using the following smoothing operator:

$$g(\alpha,\beta,\gamma)^{(n)} = \sum_{k=-1}^{k=1}\sum_{j=-1}^{j=1}\sum_{i=-1}^{i=1} w(i^2+j^2+k^2) \times g(\alpha+i,\beta+j,\gamma+k)^{(n-1)} \tag{34}$$

with

$$w(0) = 8/27, \tag{35}$$

$$w(1) = 2/27, \tag{36}$$

$$w(2) = 1/54, \tag{37}$$

$$w(3) = 1/216, \tag{38}$$

where $w(i^2+j^2+k^2)$ are the standard weights of the D3Q27 lattice and $g(x,y,z)$ is the fluid-solid binary matrix. In this research the solid matrix is smoothed for three iterations. Then the normal $\mathbf{n}_w$ to the solid matrix at the fluid lattice sites near the boundary are estimated as the gradient of the smoothed image, i.e., $\mathbf{n}_w(\alpha,\beta,\gamma) = \nabla g(\alpha,\beta,\gamma)^{(3)}$. All this computational work can be done in preprocessing before the main lattice Boltzmann time integration loop. The gradient of the smoothed image is stored in the computer memory and the vector $\mathbf{n}_w$ is called whenever it is needed in the wetting boundary condition. Note that if the gray image from the micro computed tomography scan is available, this smoothing operation is not necessarily required as the gradient could be directly computed from the gray image. However, an approximate binary fluid-solid image would still be required to do a simulation with this LBM.

III. NUMERICAL SIMULATION

This CGM has been showed to be compatible with many solutions of hydrodynamic fluid-fluid interaction problems, namely planar interface [76]; Laplace law [53]; two-phase Couette flow [39]; two-phase spinodal decomposition growth law [42]; oscillating plate [42]; Zalesak disk [42]; 2D capillary wave [42]; 2D oscillating bubble [42]; two-phase Poiseuille flow [41]; two-phase hydrostatic pressure [41]; 2D bubble subject to Archimedes force [41]; 2D capillary-gravity wave [41]; and 2D static contact angles on a curved geometry [44], among others which may use a variant of the CGM.

The proposed extensions (wetting boundary condition) to the CGM are validated against the three-dimensional Jurin and Washburn laws. The CGM is also further validated against a theoretical solution of a 3D capillary wave. Then, more complex two-phase flows in porous media are studied and discussed.

A. Jurin's law

1. Physical and numerical description

a. Continuous physical space. The setting of the Jurin law test is explained below. The domain of interest consists of the box $\mathcal{B}$:

$$\mathcal{B} = \{(x,y,z) \in [-L/2,L/2] \times [-W/2,W/2] \times [-H/2,H/2]\} \tag{39}$$

in which the following solid object $\mathcal{O}$ is immersed into the box $\mathcal{B}$:

$$\mathcal{O} = \mathcal{O}_1 \cap \mathcal{O}_2, \tag{40}$$

$$\mathcal{O}_1 = \{(x,y,z) \in \mathcal{B} : R^2 \leqslant x^2 + ay^2 \leqslant (R+t)^2\}, \tag{41}$$

$$\mathcal{O}_2 = \{(x,y,z) \in \mathcal{B} : -3H/8 \leqslant z \leqslant +3H/8\}. \tag{42}$$

In Eq. (41), the coefficient a is equal either to 0 or 1. The case with $a = 0$ corresponds to the two-dimensional Jurin law between two infinite plates while the case with $a = 1$ corresponds to the three-dimensional Jurin law which involves a three-dimensional tube. The half distance between the plates or the radius of the tube is denoted R. The value t corresponds to the thickness of the plates or the tube.

The object $\mathcal{O}_1$ can also (not necessarily) be subject to three-dimensional rotations:

$$\begin{pmatrix} x' \\ y' \\ z' \end{pmatrix} = \mathbf{R} \begin{pmatrix} x \\ y \\ z \end{pmatrix} \tag{43}$$

with the rotational matrix $\mathbf{R} = \mathbf{R}_\alpha(\theta_\alpha)\mathbf{R}_\beta(\theta_\beta)\mathbf{R}_\gamma(\theta_\gamma)$. The matrices $\mathbf{R}_\alpha(\theta_\alpha)$, $\mathbf{R}_\beta(\theta_\beta)$, and $\mathbf{R}_\gamma(\theta_\gamma)$ are two-dimensional rotational matrices around a given coordinate axis. The indexes α, β, and γ therefore correspond to one of the coordinate axes x, y, or z. The point is that rotations are not commutative and could be made in a different order for which the result is different. Following the right-hand rule, the basic rotational matrices are respectively

$$R_x(\theta_x) = \begin{pmatrix} 1 & 0 & 0 \\ 0 & \cos(\theta_x) & -\sin(\theta_x) \\ 0 & \sin(\theta_x) & \cos(\theta_x) \end{pmatrix}, \tag{44}$$

$$R_y(\theta_y) = \begin{pmatrix} \cos(\theta_y) & 0 & \sin(\theta_y) \\ 0 & 1 & 0 \\ -\sin(\theta_y) & 0 & \cos(\theta_y) \end{pmatrix}, \tag{45}$$

$$R_z(\theta_z) = \begin{pmatrix} \cos(\theta_z) & -\sin(\theta_z) & 0 \\ \sin(\theta_z) & \cos(\theta_z) & 0 \\ 0 & 0 & 1 \end{pmatrix}. \tag{46}$$

Note that in the two-dimensional case, i.e., $a = 0$, the rotational matrices are not considered which means $\theta_x = \theta_y = \theta_z = 0$.

The top ($z = H/2$) and bottom ($z = -H/2$) planes of the box $\mathcal{B}$ are solid no-slip boundaries while for simplicity periodic boundary condition are used in the other directions. The computational domain is filled with two immiscible fluids. Initially, the "bottom" fluid fills the lower half of the domain while the "top" fluid fills the upper half. The bottom fluid has an initial density ρ_B^0 and a kinematic viscosity ν_B while the top fluid has an initial density ρ_T^0 and a kinematic viscosity ν_T. The interfacial tension σ at the interface of the two immiscible fluids is also taken into account as well as the contact angle θ_c at the fluids-solid boundary. The gravity acceleration g is also an important parameter to be considered.

b. Theoretical consideration. The goal of the experiment is to study at steady state the differential height h between the inside and outside meniscus predicted by Jurin's law as a function of these parameters. In our setting, the differential rise or fall capillary heights h is a function of the following parameters:

$$h = \widetilde{\mathcal{F}}\big(L,W,H,t,R,\sigma,\nu_B,\nu_T,\rho_B^0,\rho_T^0, g,\theta_c,\theta_x,\theta_y,\theta_z,\alpha,\beta,\gamma,a\big). \tag{47}$$

According to a dimensional analysis by Refs. [86,87], the following dimensionless formulation appears:

$$\frac{h}{R} = \mathcal{F}(W/L,H/L,t/L,R/L,\frac{\rho_T^0}{\rho_B^0},\frac{\nu_T}{\nu_B},\text{La}, \text{Bo},\theta_c,\theta_x,\theta_y,\theta_z,\alpha,\beta,\gamma,a), \tag{48}$$

where the Laplace, La, and Bond, Bo, numbers are respectively

$$\text{La} = \frac{\sigma R}{\rho_B^0 \nu_B^2}, \tag{49}$$

$$\text{Bo} = \frac{\left(\rho_B^0 - \rho_T^0\right) R^2 g}{\sigma}. \tag{50}$$

Jurin's law states that the function $\mathcal{F}$ depends only on a, θ_c, and Bo such that

$$\frac{h}{R}\text{Bo} = (a+1)\cos\theta_c. \tag{51}$$

The following additional hypothesis needs also to be taken into account. Experimental analysis predicts well the capillary rise or fall as long as the geometry rotations are not too large [63], i.e., less than 50°. It should be noted that Jurin's law is valid provided that the radius R is much less than the capillary length, or said differently, smaller the Bond number. Here, because of the periodic boundary condition, the length L must also be much greater than the radius R to avoid capillary competition between the periodic plates or tubes, which Jurin's law does not take into account. The wall's surface is also considered ideal and exempt of any roughness or waviness.

In a full analysis of the problem, all dimensionless numbers should be taken into account. This is beyond the scope of this research, so for simplicity, the following dimensionless numbers are kept constant: $W/L = 1$, $H/L = 1$, $t/L = 1/64$, $R/L = 1/32$, and $\frac{\rho_B^0}{\rho_T^0} = 10$. Our numerical analysis will thus concentrate on varying the other dimensionless parameters. Once all dimensionless parameters are chosen, there are some underlying parameters that are still free to vary, which we set as $L = 1$, $\nu_B = 1/20$, and $\rho_B^0 = 1000$. It is very important to note that since these choices lead to a constant height H for all simulations, this limits the range of the Bond number that can be simulated, because the maximum capillary rise or fall h depends on the Bond number. Therefore, in order to be consistent with the domain size, we respectively fix in two and three dimensions the numbers Bo = 0.2 and Bo = 0.4.

c. Discrete physical space. The problem is discretized with the following number of lattice sites:

$$N_x = s N_x^{\text{Coarse}}, \tag{52}$$

$$N_y = \begin{cases} 4, & a = 0 \\ N_x, & a = 1 \end{cases}, \tag{53}$$

$$N_z = N_x + 2, \tag{54}$$

where s is a lattice size parameter used to describe different lattice resolutions. In the 2D case with $a = 0$, four lattice sites are used, because our PALABOS code is in fact a three-dimensional implementation and requires in this case a minimum thickness of four lattice sites. We use $N_x^{\text{Coarse}} = 80$ and as usual in the LBM, the discrete physical spacing $\Delta x = L/N_x$ is equal in all three space directions. The physical time is adjusted to the space discretization according to a diffusive limit $\Delta t = \Delta x^2$, in order to respect the condition of fluid incompressibility [69]. The D3Q19 lattice is used for this test case.

d. Numerical setup. The bottom and top fluids are initialized with an equilibrium distribution at zero velocity with bottom fluid where $H < 0$ and top fluid where $H > 0$. The single-relaxation-time operator is used, i.e., $\chi = 1$. The standard full-way bounce back rule is used for all solid lattice sites in $\mathbf{X}_S$. The solid lattice sites are composed of the first and last lattice plane in the vertical direction as well as the interior of the immersed object $\mathcal{O}$. To evaluate the color $\mathbf{F}$ and the density $\nabla\rho$ gradients, 3D fourth-order isotropic discretizations [88] are used on all lattice sites, except for the lattice sites in $\mathbf{X}_W$ where a standard 1D forward, backward, and/or centered discrete gradient [89] is used. Note that the previously described wetting boundary condition in Sec. II E is also applied before the perturbation step. Others model parameters [77] are $\eta = 0.2$, $\beta^* = 1$, and $\Delta x^* = L/N_x^{\text{Coarse}}$.

e. Evaluation of the steady-state and numerical height h. The numerical differential height h is approximated during the simulation with an automated procedure. We computed the center of mass of the bottom fluid along the z-axis column $\mathcal{C}_{\text{i}}$ (inside the tube) and along the vertical-axis column $\mathcal{C}_{\text{o}}$ located at $(x,y) = (-L/2,-W/2)$ (outside of the tube). These centers of masses z_{index} can be approximated with

$$z_{\text{index}} = \sum_{(x,y,z)\in\mathcal{C}_{\text{index}}} m_B z \Big/ \sum_{(x,y,z)\in\mathcal{C}_{\text{index}}} m_B, \qquad (55)$$

where $m_B = \rho_B \Delta x^3$ is the mass of the bottom fluid and the index is either i or o for the inside or outside column. The approximated numerical differential height is then defined as $h = 2(z_{\text{i}} - z_{\text{o}})$. The steady state is considered reached when the relative difference of the dimensionless quantity $h\text{Bo}/R$ is less than 10^{-5} between a time interval of $\delta t = 1$. For the simulations where there is a rotation of the solid object $\mathcal{O}_1$, the numerical differential height is computed manually with the aid of the free software PARAVIEW [90]. In PARAVIEW, the inside and outside heights are approximated with the contour of the function $(\rho_B - \rho_T)/(\rho_B + \rho_T) = 0$. The main difference is that it is the central axis of the rotated tube that is considered. Both approaches to measure the differential height lead to very similar results, however, we prefer to extract the numerical differential heights with an automated procedure whenever it is possible. The simulation is stopped when $t = 20$ in the rotated case, which is a time the flow was deemed to have reached steady state.

2. *Discussion of the results*

Figure 2 shows the dimensionless quantity $\frac{h}{R}\text{Bo}$ versus the analytical two-dimensional Jurin law as a function of the viscosity ratio, the Laplace number, the contact angle, and a lattice resolution $s = 2$. The results show that the proposed method is accurate for a contact angle between 45° and 135°. The errors are nonsymmetric for contact angles lower than 45° compared to contact angle higher than 135°. This is because of the density and viscosity ratios. From a geometrical point of view, it is very difficult to represent the correct interface curvature between the plates with only ten lattice sites when the contact angle is far away from 90°.

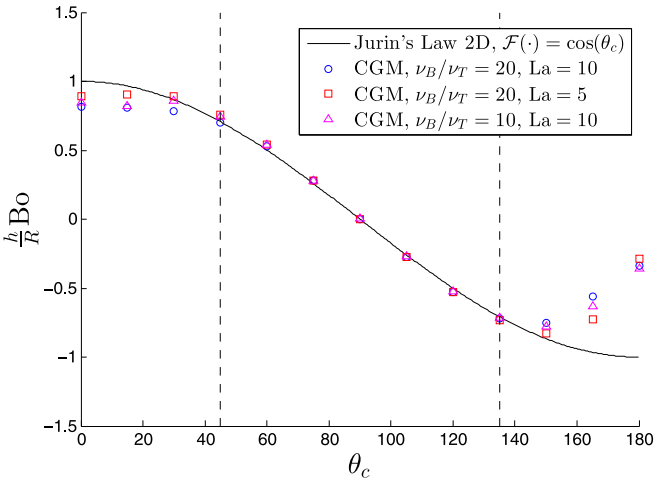

FIG. 2. Dimensionless quantity $\frac{h}{R}\text{Bo}$ as function of the viscosity ratio ν_B/ν_T, the Laplace number La, and the contact angle θ_c compared to the analytical two-dimensional Jurin law. Note that the lattice resolution $s = 2$.

Figure 3 shows the results for one set of parameters, but with increasing lattice resolution. It is possible to see that the accuracy is increasing, but the model is still not completely able to automatically capture Jurin's law correctly for the more extreme wetting or nonwetting fluid situation. This test case thus gives a range of contact angles where the proposed algorithm can be considered valid.

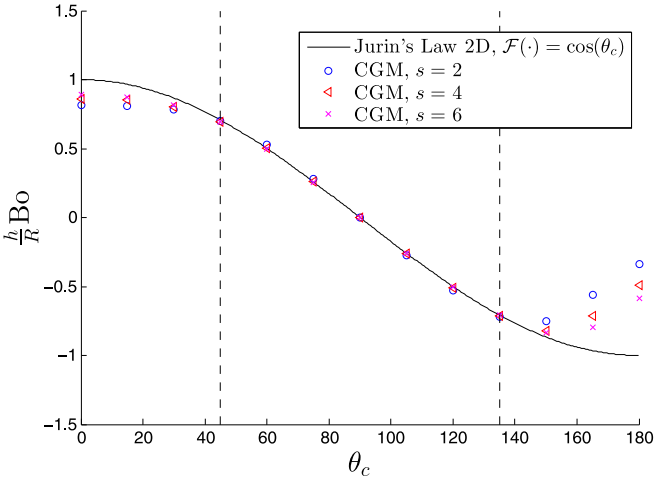

FIG. 3. Dimensionless quantity $\frac{h}{R}\text{Bo}$ as function of the contact angle θ_c and the lattice resolution s compared to the analytical two-dimensional Jurin law. Note that the viscosity ratio $\nu_B/\nu_T = 20$ and the Laplace number La = 10.

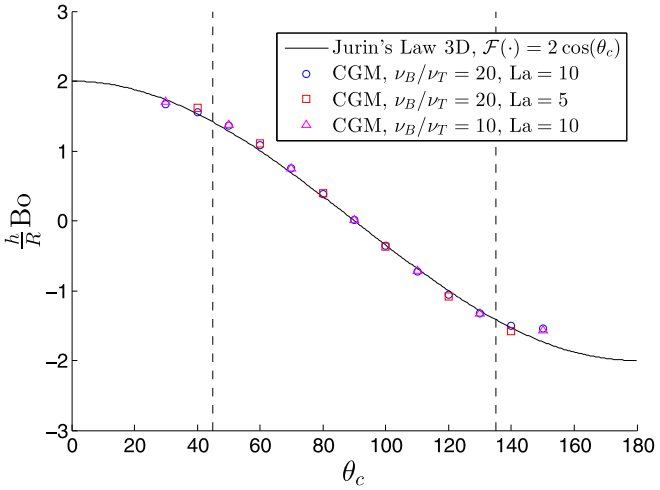

FIG. 4. Dimensionless quantity $\frac{h}{R}$Bo as function of the viscosity ratio ν_B/ν_T, the Laplace number La, and the contact angle θ_c compared to the analytical three-dimensional Jurin law. Note that the lattice resolution $s = 2$.

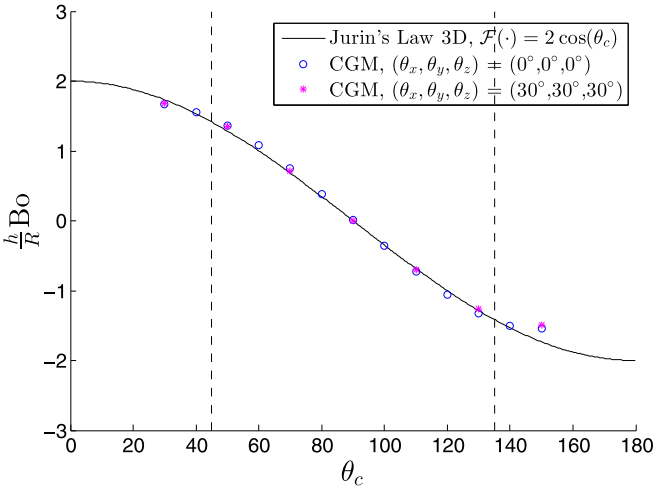

FIG. 6. Dimensionless quantity $\frac{h}{R}$Bo as function of the contact angle θ_c and the geometry rotations $(\theta_x,\theta_y,\theta_z)$ compared to the analytical three-dimensional Jurin law. Note that the lattice resolution $s = 2$, the viscosity ratio $\nu_B/\nu_T = 20$, and the Laplace number La $= 10$.

Figure 4 shows the same results as in Fig. 2, but for the three-dimensional case. The three-dimensional Jurin law is much more difficult to solve numerically as it also involves the effect of the three-dimensional tube geometry. With a lattice resolution of $s = 2$, the diameter of the tube is equal to ten lattice sites which one could argue to be a minimum required to represent the solid circular geometry of the tube with a staircase approximation. Fortunately, the results for the contact angles between 45° and 135° are similarly as good as in the two-dimensional case.

To increase further the difficulty of this numerical validation, the tube is rotated by angles $(\theta_x,\theta_y,\theta_z) = (30°,30°,30°)$, as illustrated in Fig. 5 for a contact angle of 45°. On this figure, the capillary rise predicted by Jurin's law is clearly visible. This additional rotation increases much more the effect of the staircase approximation, but the wetting boundary condition

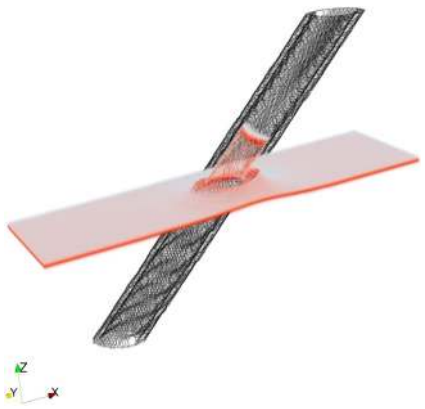

FIG. 5. Graphical representation of the rotated tube geometry with the bottom fluid highlight. As predicted by Jurin's law, the capillary rise is clearly visible. Note that the lattice resolution $s = 2$, the viscosity ratio $\nu_B/\nu_T = 20$, the Laplace number La $= 10$, the contact angle $\theta_c = 45°$, and the geometry rotations $(\theta_x,\theta_y,\theta_z) = (30°,30°,30°)$.

algorithm does not seem to be really affected by this additional difficulty. Indeed, as shown in Fig. 6 for different contact angles, the numerical results for the inclined tube are pretty much the same as in the noninclined case. This is in agreement with the theory presented by Barozzi and Angeli [63] that state that Jurin's law is still accurate for small rotations.

It is important to note that those numerical tests are extremely difficult as the solver needs to correctly balance the capillary, pressure, viscous, and gravity forces as well as to capture sufficiently well the correct geometrical shape of the tube and the interface's meniscus inside and outside the tube. Overall, these numerical tests show that the proposed model is appropriate for modeling the full three-dimensional Jurin law for contact angle between 45° and 135°, and this even with a relatively numerically coarse tube diameter. It should be noted that Jurin's law only tests the steady state of the numerical algorithm, so the next test case concerns Washburn's law where the model is tested in an unsteady regime.

B. Washburn's law

1. Physical and numerical description

a. Continuous physical space. The setting of the Washburn law test is explained below. Similarly as with the Jurin law test, the domain of interest consists of the box $\mathcal{B}$:

$$\mathcal{B} = \{(x,y,z) \in [-L_I, L + L_O] \times [-R/2, R/2] \times [-R/2, R/2]\} \tag{56}$$

in which the following solid object $\mathcal{O}$ is immersed into the box $\mathcal{B}$:

$$\mathcal{O} = \mathcal{O}_1 \cap \mathcal{O}_2, \tag{57}$$

$$\mathcal{O}_1 = \{(x,y,z) \in \mathcal{B} : z^2 + y^2 \geqslant R^2\}, \tag{58}$$

$$\mathcal{O}_2 = \{(x,y,z) \in \mathcal{B} : 0 \leqslant x \leqslant L\}. \tag{59}$$

This configuration corresponds to a tube of radius R and length L with two additional fully fluid domains of length $L_I = L_O$ that extend on both ends of the tube. The center of the tube is aligned with the x axis and starts at $x = 0$. The inlet ($x = -L_I$) and the outlet ($x = L + L_O$) are density boundary conditions while periodic boundary conditions are used for the other directions. The solid boundary is modeled with a no-slip condition.

The computational domain is filled with two immiscible fluids. Initially, the "inlet" fluid fills the inlet zone, i.e., $-L_I < x < 0$, while the "outlet" fluid fills the rest. The inlet fluid has an initial density ρ_I^0 and a dynamic viscosity μ_I while the outlet fluid has an initial density ρ_O^0 and a dynamic viscosity μ_O. The interfacial tension σ at the interface of the two immiscible fluids is also taken into account as well as the contact angle θ_c at the fluid-solid boundary. The gravity acceleration g is not an important parameter to be considered for this horizontal tube and is set to zero.

b. Theoretical consideration. The goal of the experiment is to study the time dependence of the position of the fluid's interface. Indeed, because of the presence of the contact angle imposed on the tube boundary, the interface is deformed and a capillary pressure will appear at the fluid interface and it will start to move. To make sure the interface is moving toward the inside of the tube, the pressure is set to be constant and equal on both ends of the domain. The inlet fluid also needs to be the wetting fluid as well as being more viscous than the outlet fluid, i.e., $\mu_I > \mu_O$. Washburn's original analytical solution [65] is rewritten in a dimensionless form:

$$l^* = -\left(\frac{\mu_O}{\mu_I - \mu_O}\right) + \sqrt{\left(\frac{\mu_O}{\mu_I - \mu_O}\right)^2 + \left(\frac{1}{2}\frac{R}{L}\cos\theta_c\right)t^*}, \tag{60}$$

where $l^* = \frac{l}{L}$ is the dimensionless position of the interface along the tube and $t^* = \frac{\sigma}{(\mu_I - \mu_O)L}t$ is the dimensionless time. The surface of the wall is also considered ideal such that any roughness and waviness are absent. We may note that if the outer fluid dynamic viscosity is negligible, i.e., $\mu_O \ll \mu_I$, the analytical solution clearly illustrates the widely known proportion relation $l^* \propto \sqrt{t^*}$.

In our setting, the dimensionless parameters that we choose to include are θ_c, L/R, L_I/L, L_O/L, μ_I/μ_O, ρ_I/ρ_O, and $\mathrm{La} = \sigma R\rho_I/\mu_I^2$. For simplicity, we set constant the following dimensionless numbers: $L/R = 20$, $\mathrm{La} = 1$, and $L_I/L = L_O/L = 22/100$. There are some underlying parameters that are still free to vary which we set as $R = 0.000\,02$, $\nu_I = 1/6$, and $\rho_I^0 = 998.2$. In the end, only the contact angle θ_c, the dynamic viscosity μ_I/μ_O, and the density ρ_I/ρ_O ratios are free to vary.

To provide a better understanding of the setting of the Washburn test case, Fig. 7 shows visually the results of a simulation example. A capillary intrusion of water into a single cylindrical pore initially filled with hexane is illustrated at the dimensionless time $t^* \approx 48.3$. The water-hexane density and dynamic viscosity ratios are $\rho_I/\rho_O = 1.5094$ and $\mu_I/\mu_O = 3.2277$. The water-solid contact angle is 40°.

c. Numerical setup. The domain is discretized such that the radius of the tube R contains $N^{\mathrm{Coarse}} = 5$ fluid lattice sites. In total, the full lattice contains $144 \times 12 \times 12$ sites. One may note that this is a very coarse lattice. This is done intentionally. Indeed, for modeling flows in porous media, it is needed to be able to capture the imbibition process as accurately as possible on the coarser possible grid. This is similar as in the Jurin law test where the radius of the tube was also of five lattice sites with $s = 2$. However, the radius also needs to be large enough in lattice units so that the geometry represents a circular tube. The standard full-way bounce back rule is used for all solid lattice sites in $\mathbf{X}_S$. The physical space step $\Delta x = 2R/(N_y - 2)$ is equal in all three space directions. The physical time is adjusted to the space discretization according to a diffusive limit $\Delta t = \Delta x^2$. The inlet and outlet fluids are initialized with an equilibrium distribution at zero velocity. To evaluate the color $\mathbf{F}$ and the density $\nabla\rho$ gradients, 3D fourth-order isotropic discretizations [88] are used on all lattice sites, except for the lattice sites in $\mathbf{X}_W$ where a standard 1D forward, backward, and/or centered discrete gradient [89] is used. These gradients are also set to zero on the inlet and outlet boundary lattice sites in $\mathbf{X}_E$. The previously described wetting boundary condition in Sec. II E is also applied before the perturbation step. On the inlet and outlet boundary and as described in Sec. II D, regularized density boundary conditions are used such that ρ_I^0 and ρ_O^0 are respectively imposed. Since the numerical position of the solid boundary might be slightly affected by the value of the lattice Boltzmann viscosity, the multiple-relaxation-time operator is used and the relaxation parameters are set as in Ref. [91] using the set B. Very recent study seems to point out [92], however, that single-relaxation-time may be sufficient to obtain accurate results and this, as long as the Knudsen number is low. Other parameters [77] are $\eta = 0.2$, $\beta^* = 1$, and $\Delta x^* = 2R/(N^{\mathrm{Coarse}} - 2)$. The D3Q19 lattice is used for this test case.

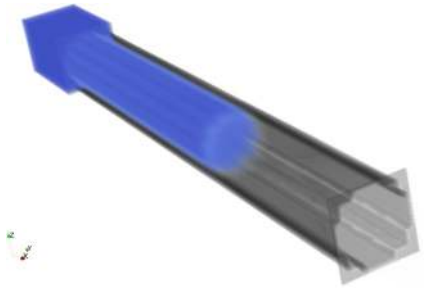

FIG. 7. Capillary intrusion of water into a single cylindrical pore initially filled with hexane, i.e., $\rho_I/\rho_O = 1.5094$ and $\mu_I/\mu_O = 3.2277$. The water-solid contact angle is 40° and $t^* \approx 48.3$.

d. Evaluation of the dimensionless position l^*. The dimensionless position of the interface is approximated as follows. First, a color function is defined:

$$\psi = \frac{\rho_I}{\rho_I + \rho_O}. \tag{61}$$

This function takes a value of 1 or 0 depending on whether the lattice site contains only inlet or outlet fluid respectively. At the interface the value will be between 1 and 0 relative to the proportion of each fluid. The capillary saturation of the inlet fluid into the tube is approximated by the summation of ψ inside the tube divided by the number of fluid lattice sites that are also strictly inside the tube. In our simple case, it is

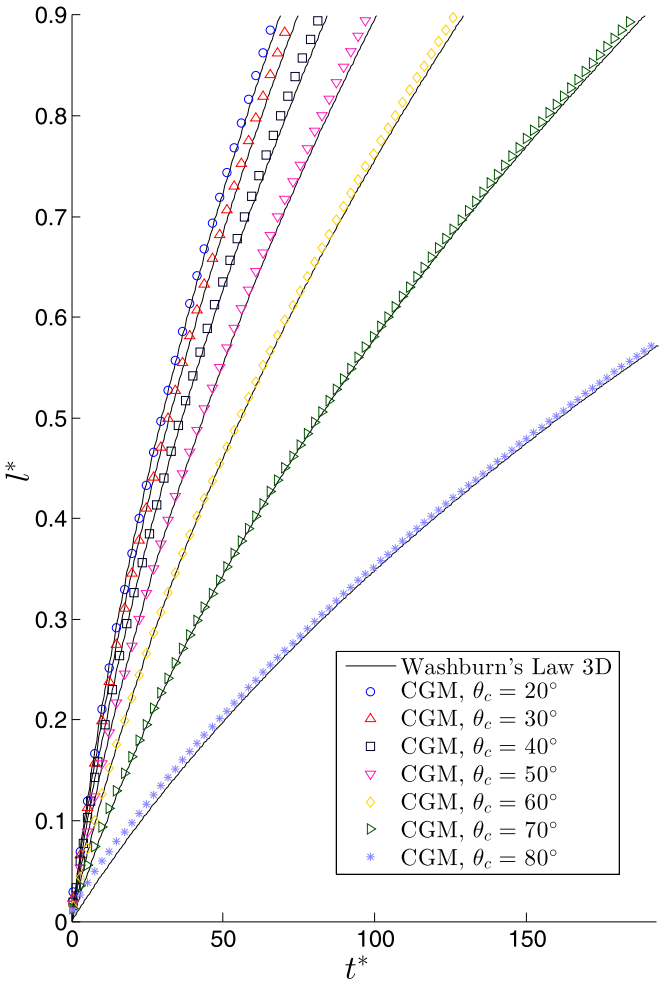

FIG. 8. Dimensionless position of the fluid interface l^* into the single cylindrical pore as function of the dimensionless time t^* and the contact angle θ_c. The numerical results of the proposed lattice Boltzmann color-gradient method are compared to the analytical three-dimensional Washburn law. Water-hexane density and viscosity ratios are simulated, i.e., $\rho_I/\rho_O = 1.5094$ and $\mu_I/\mu_O = 3.2277$. These simulations correspond to a capillary intrusion of water into a single cylindrical pore filled initially with hexane.

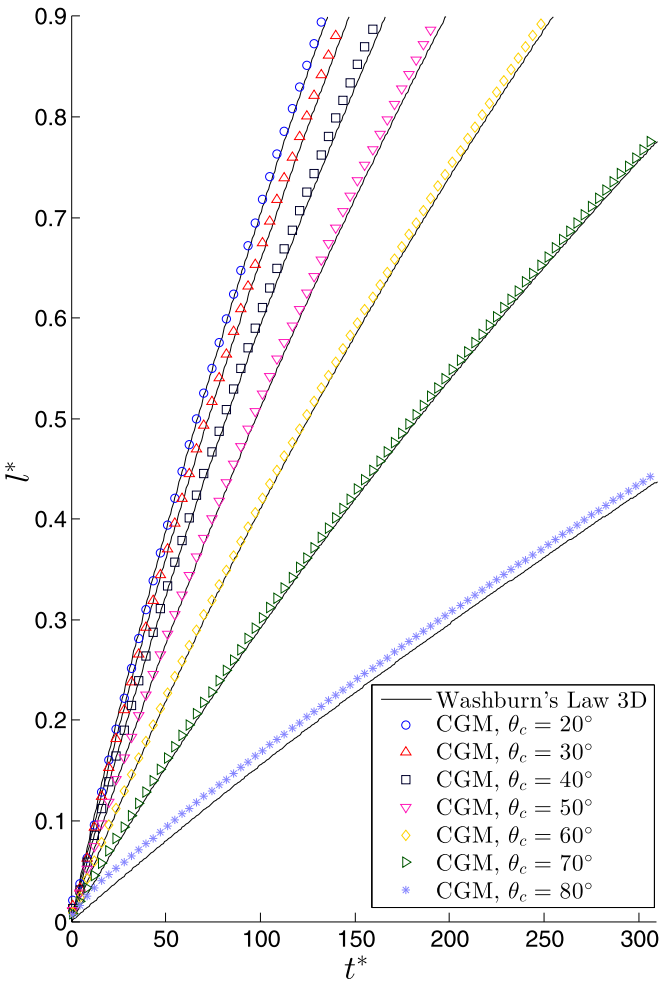

FIG. 9. Dimensionless position of the fluid interface l^* into the single cylindrical pore as function of the dimensionless time t^* and the contact angle θ_c. The numerical results of the proposed lattice Boltzmann color-gradient method are compared to the analytical three-dimensional Washburn law. Water-trichloroethylene density and viscosity ratios are simulated, i.e., $\rho_I/\rho_O = 0.6828$ and $\mu_I/\mu_O = 1.7583$. These simulations correspond to a capillary intrusion of water into a single cylindrical pore filled initially with trichloroethylene.

clear that the capillary saturation can be used to estimate the dimensionless position l^* of the interface in the tube.

2. *Discussion of the results*

Figures 8–10 show the dimensionless position of the fluid interface l^* as functions of the dimensionless time t^* and the contact angle θ_c. Three types of density and viscosity ratios were respectively considered:

(1) water to hexane where $\rho_I/\rho_O = 1.5094$ and $\mu_I/\mu_O = 3.2277$;

(2) water to trichloroethylene where $\rho_I/\rho_O = 0.6828$ and $\mu_I/\mu_O = 1.7583$ [93]; and

(3) dimensionless ratios where $\rho_I/\rho_O = 10$ and $\mu_I/\mu_O = 30$.

The second test with the lower density at the inlet is slightly more difficult than the first test while the last one is the most difficult because of a much larger density and viscosity ratio. The last test is difficult enough that it encompasses most types of liquid-liquid interfaces. There may be a small discrepancy between the numerical and theoretical results. Indeed, occasionally the numerical dots are not directly over the analytic curve. This can be explained, in part, because the theory does not take into account the initial condition of the numerical setting. Indeed, for simplicity, the initial interface has a contact angle of 90° with the boundary and will therefore need to relax to the contact angle prescribed by the wetting boundary condition. This creates an initial capillary wave at the tube entry that perturbs the initial interface position. It is also clear that the last test generate the largest numerical errors. However, all in all, the three-dimensional Washburn law is well described by the proposed two-phase color-gradient model for a wide range of contact angles, density, and viscosity ratios. This confirms that the model is adequate for capturing unsteady capillary intrusion into a simple pore even if the

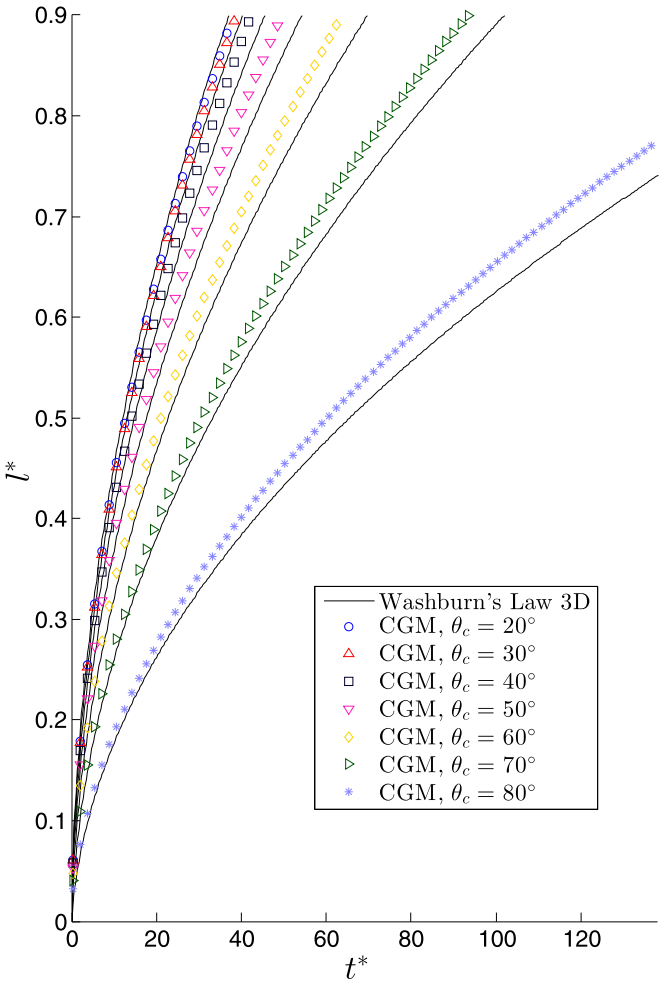

FIG. 10. Dimensionless position of the fluid interface l^* into the single cylindrical pore as function of the dimensionless time t^* and the contact angle θ_c. The numerical results of the proposed CGM are compared to the analytical three-dimensional Washburn law. The density and viscosity ratios are respectively, i.e., $\rho_I/\rho_O = 10$ and $\mu_I/\mu_O = 30$.

lattice resolution is very coarse. It also confirms the validity of the approach taken to model the wetting boundary conditions.

C. Three-dimensional capillary wave

1. Physical and numerical description

a. Continuous physical space. The setting of the capillary wave test case is explained below. The domain of interest consists of the box $\mathcal{B}$:

$$\mathcal{B} = \{(x,y,z) \in [0,L] \times [0,W] \times [0,H]\}. \tag{62}$$

A perturbed thick sheet of fluid $\mathcal{T}$ is placed in between another immiscible fluid and is located at

$$\mathcal{T} = \{(x,y,z) \in \mathcal{B} : H/4 < z - h_p < 3H/4\} \tag{63}$$

with

$$h_p = \frac{h}{2}\cos\left[2\pi(x - L/2)/\lambda\right] + \frac{h}{2}\cos\left[2\pi(y - W/2)/\lambda\right], \tag{64}$$

where h is the initial amplitude and λ is the wavelength of the perturbation. The fluid sheet is the blue fluid with an initial density ρ_b^0 and a dynamic viscosity μ_b while the medium fluid is the red fluid with an initial density ρ_r^0 and a dynamic viscosity μ_r. The interfacial tension σ at the interface of the two immiscible fluids is also taken into account. For simplicity, periodic boundary conditions are used in all directions. The experiment consists to study the angular frequency ω of this surface wave as a function of these parameters:

$$\omega = \mathcal{F}\left(L,W,H,h,\lambda,\sigma,\mu_r,\mu_b,\rho_r^0,\rho_b^0\right). \tag{65}$$

The function $\mathcal{F}$ is an unknown functional and a dimensional analysis leads to the following Pi groups:

$$\mathrm{Re} = \mathcal{G}\left(\frac{L}{\lambda},\frac{W}{\lambda},\frac{H}{\lambda},\frac{\lambda}{h},a,b,\Gamma\right), \tag{66}$$

where the function $\mathcal{G}$ is another unknown functional and

$$\mathrm{Re} = \frac{\omega\lambda^2\rho_r^0}{\mu_r}, \tag{67}$$

$$a = \frac{\mu_b}{\mu_b + \mu_r}, \tag{68}$$

$$b = \frac{\rho_b^0}{\rho_b^0 + \rho_r^0}, \tag{69}$$

$$\Gamma = \frac{\sigma}{k}\frac{\left(\rho_r^0 + \rho_b^0\right)}{(\mu_r + \mu_b)^2}. \tag{70}$$

In this particular case, Re is the oscillatory Reynolds number, a and b are dimensionless numbers related to the density and dynamic viscosity ratios. We also introduced the dimensionless number Γ which is a quantity related with the long wavelength limit, i.e., when $\Gamma \gg 1$. Note that $k = 2\pi/\lambda$ is the wave number. Again, in this case, for a full understanding of the problem all dimensionless numbers should be taken into account. However, since our main goal is to compare a numerical angular frequency with a theoretical one, some simplification needs to be done. The following dimensionless numbers are set as constant, i.e., the ratios $L/\lambda = 1$, $W/\lambda = 1$, $H/\lambda = 4$, and $\lambda/h = 10$. This leads to

$$\mathrm{Re} = \tilde{\mathcal{G}}(a,b,\Gamma). \tag{71}$$

In the proposed setting, there are some underlying parameters that are still free to vary and are set as $\lambda = 1$, $\mu_r = 1/100$, and $\rho_r^0 = 1$.

b. Theoretical consideration. A theoretical dispersion relation exists for surface waves on an interface between two liquids [66]. When the gravitational acceleration is neglected, the dispersion relation for the angular frequency ω is

$$0 = +(1 - i1\omega\tau)^2 + (\omega_1\tau)^2 - a\sqrt{1 - i2\omega\tau a/b} - (1 - a)\sqrt{1 - i2\omega\tau(1 - b)/(1 - a)}, \tag{72}$$

where $i = \sqrt{-1}$ is the imaginary number and

$$\tau = \frac{\rho_r^0 + \rho_b^0}{2k^2(\mu_r + \mu_b)}, \tag{73}$$

$$\omega_1^2 = \frac{\sigma k^3}{\rho_r^0 + \rho_b^0}. \tag{74}$$

Note that the long wavelength limit is when $(2\omega_1\tau)^2 = \Gamma \gg 1$. Given the necessary parameters of a simulation, this expression is solved to find ω and the theoretical oscillatory Reynolds number is deduced. The latter is usually a complex number where the real part corresponds to the angular frequency of oscillation of the surface wave while the imaginary part is linked to its damping rate. It should be noted that this theoretical dispersion relation is for waves in an infinite medium where the boundary and initial condition do not affect the damped periodical theoretical solution. Our numerical setting is obviously not exactly as this theoretical case, but the numerical setting is near enough that it is still possible to find a correlation between the theoretical and numerical solutions.

c. Discrete physical space. The problem is discretized as follows. Let us define again a lattice density size parameters s. The number of lattice sites required to discretized the problem is defined as

$$N_x = (L/\lambda)N^{\text{Coarse}}s, \tag{75}$$

$$N_y = (W/L)N_x, \tag{76}$$

$$N_z = (H/L)N_x. \tag{77}$$

For this test case, we used $N^{\text{Coarse}} = 50$. The spacing steps $\Delta x = \Delta y = \Delta z = \lambda/N_x$ discretize the computational domain, and the time step $\Delta t = \Delta x^2$ discretizes the time domain.

d. Numerical setup. The red and blue fluids are initialized with the zero velocity equilibrium distribution such that the blue fluid is initially located inside the sheet $\mathcal{T}$ with strictly only red fluid outside and strictly only blue fluid inside the initial sheet $\mathcal{T}$. The multiple-relaxation-time operator is used with $\chi = 4/5$. Concerning the gradient's numerical evaluation, the 3D fourth order isotropic discretization [88] is used for all lattice sites. The other parameters [77] are $\eta = 0.2$, $\beta^* = 1$, and $\Delta x^* = \lambda/N_x^{\text{Coarse}}$. The D3Q19 lattice is used.

e. Numerical evaluation of the Reynolds number Re. Let us define the center of mass of the blue fluid which is located on the central axis, i.e., $x = L/2$ and $y = W/2$. The height of the center of mass h_c is probed every five time steps and extracted from the simulation. The function h_c is a one-dimensional time dependent function where successive local maximum and minimum appear. After $t > 3$, we start to record the time $t_1, t_2, \ldots$, where those local extrema appear and the simulation is stopped when t_6 is achieved. The numerical period of oscillations is then approximated as $2(t_6 - t_5)$ and the real part of the numerical Reynolds number is approximated as $\Re(\text{Re}) = \frac{2\pi}{2(t_6-t_5)}\frac{\lambda^2}{\nu_r}$. As it is very difficult to precisely measure in the simulation the imaginary part of ω, we neglect all analysis concerning the imaginary part. Indeed, the oscillation amplitude is initially strongly affected by the initial condition which causes the initial damping factor to not represent the one of the periodical theoretical solution and, near the end of the simulation, the oscillation amplitude is so small that it is difficult to precisely measure the wave amplitude. This happens because the model uses a diffuse interface and it lacks spatial resolution in that domain region. Overall, this problem does not appear when measuring the oscillation frequency because the time axis is well discretized with the lattice Boltzmann method, but the same cannot be said for the spatial resolution where the oscillation amplitude needs to be measured. Maybe a local lattice refining technique would help, but this is out of scope of the present work.

2. Discussion of the results

Accurate simulation of a full three-dimensional capillary wave with this lattice Boltzmann method is an important test to validate the interaction of the pressure and capillary forces in an unsteady regime. Figure 11 shows the results of the simulations against the theoretical prediction. The real part of the oscillatory Reynolds number $\Re(\text{Re})$ is shown as a function of the relative viscosity a, the relative density b, and the dimensionless number Γ. It is clear that the numerical results match the theoretical dispersion relation (72) for a wide range of parameters. The relative viscosity a and density b are in the same range as what would be liquid-liquid interfaces. This test case thus further confirms the accuracy of this lattice Boltzmann method for simulating the dynamic of liquid-liquid capillary interfaces.

D. Regime transition in random porous media

1. Physical and numerical description

a. Continuous physical space. The setting of the regime transition test case is explained below. The domain of interest consists of the two-dimensional box $\mathcal{B}$,

$$\mathcal{B} = \{(x,z) \in [0, L + L_I + L_O] \times [0, H]\}, \tag{78}$$

in which the following random porous media object $\mathcal{O}$ is immersed into the box $\mathcal{B}$:

$$\mathcal{O} = \mathcal{O}_1 \cap \mathcal{O}_2, \tag{79}$$

$$\mathcal{O}_1 = \{(x,z) \in \mathcal{B} : 0 \leqslant z \leqslant H\}, \tag{80}$$

$$\mathcal{O}_2 = \{(x,z) \in \mathcal{B} : L_I \leqslant x \leqslant L + L_O\}. \tag{81}$$

This configuration corresponds to a random porous media $\mathcal{O}$ of length L and height H with two additional fully fluid domains of length $L_I = L_O$ that extend on both ends of the porous media.

The inlet ($x = 0$) is a velocity boundary condition and the outlet ($x = L + L_I + L_O$) is a density boundary condition. Periodic boundary conditions are used for the other directions. The solid boundary of the porous media is modeled with a no-slip condition. The porous media $\mathcal{O}$ is a random structured network of pores and throats that will be defined later.

When gravity effects can be neglected, the displacement of a nonwetting fluid in a porous medium that is otherwise saturated with a wetting fluid depends on the balance between capillary and viscous stresses, for instance, whether the nonwetting fluid will preferentially displace the wetting one

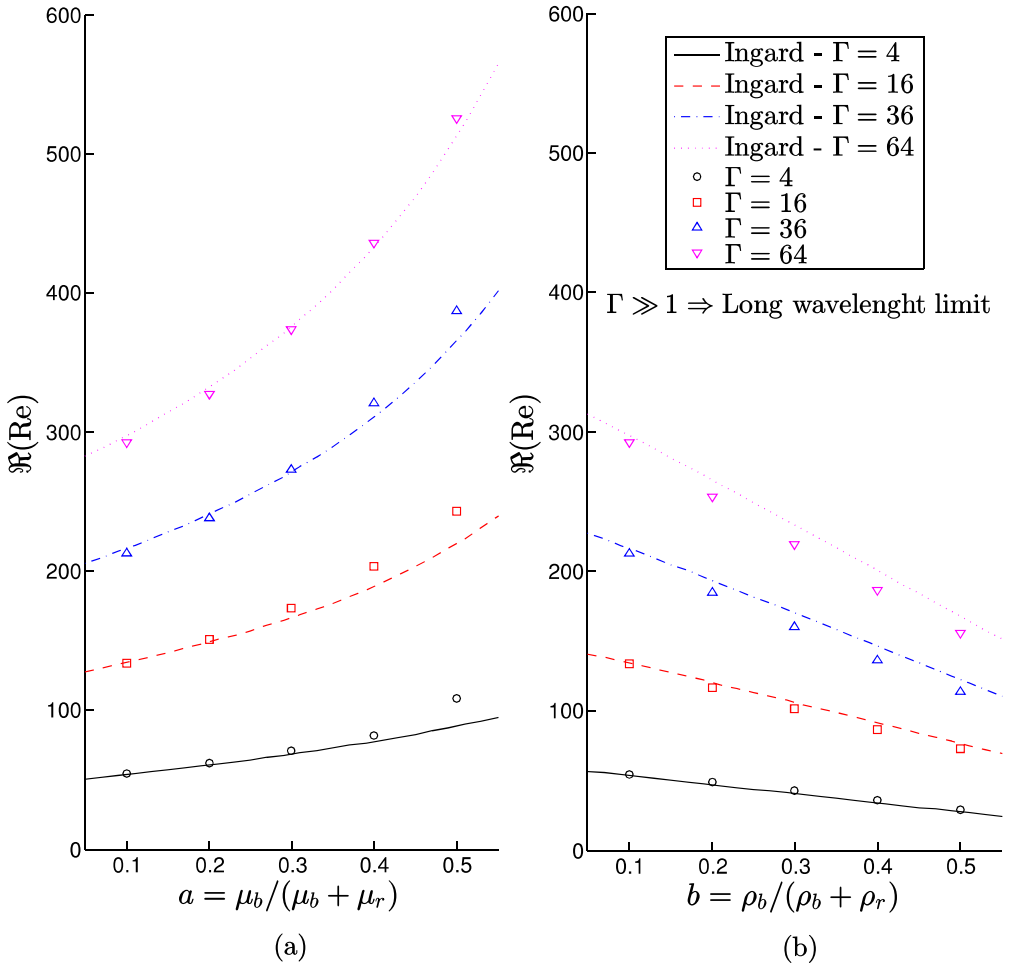

FIG. 11. Real part of the oscillatory Reynolds number $\Re(\mathrm{Re})$ as function of the relative viscosity a, the relative density b, and the dimensionless number Γ; the quantity $b = 1/10$ in the left plot and $a = 1/10$ in the right plot.

heterogeneously forming fingers like structure or will form a rather homogeneous displacing front depends on the dynamic viscosities of the injected/inlet μ_I and defending/outlet μ_O fluids, the injection rate Q, the interfacial tension between the two immiscible fluids σ and the geometrical properties of the porous medium (i.e., notably the average throat size $\overline{R}_t$). These physical parameters can be grouped into three dimensionless numbers, the viscosity ratio M, the capillary number C and the Reynolds number Re:

$$M = \frac{\mu_I}{\mu_O}, \tag{82}$$

$$C = \frac{u_I \mu_I}{\sigma |\cos(\theta_c)|}, \tag{83}$$

$$\mathrm{Re} = \frac{u_I \overline{R}_t}{\nu_I}, \tag{84}$$

where $u_I = Q/A$ is a uniform inlet velocity and A is the porous media cross-section area. The inlet fluid has an initial density ρ_I^0 while the outlet fluid has an initial density ρ_O^0. The contact angle at the fluids-solid boundary is θ_c.

b. Lenormand's phase diagram. Lenormand *et al.* [55] showed that the nonwetting fluid pattern displacement can be qualitatively inferred by knowing M and C. The authors proposed a two variable $\log_{10}(M)$ and $\log_{10}(C)$ phase diagram in which three basic patterns of nonwetting fluid invasion can be plotted; see Fig. 12. These are viscous fingering (light green), capillary fingering (light red), and stable displacement front (deep blue). Note that in their experiments, the Reynolds number is usually always very small. At high capillary numbers, if the injected nonwetting phase is more viscous than the wetting one, a stable pistonlike front displacement has to be expected. During displacement, the nonwetting phase almost completely saturates the porous medium. For example, the nonwetting fluid explores both small and high aperture throats and the saturation of the nonwetting phases can get very close to 1. On the other hand, when the viscosity of the defending wetting fluid is markedly higher than the one of the injected nonwetting one, a viscous pressure drop exerted by the defending fluid dominates and the nonwetting phase will form heterogeneous fingers parallel to the pressure gradient, i.e., the viscous fingering regime. In this case low nonwetting saturation $S \sim 0.2$ must be expected. At low capillary number of injections, i.e., $C \ll 1$, and over a wide range of viscosity ratios [i.e., $\log_{10}(M)$ higher and lower than 0] pore-by-pore capillary pressure drops dominate (i.e., capillary fingering regime) and the nonwetting fluid will tend

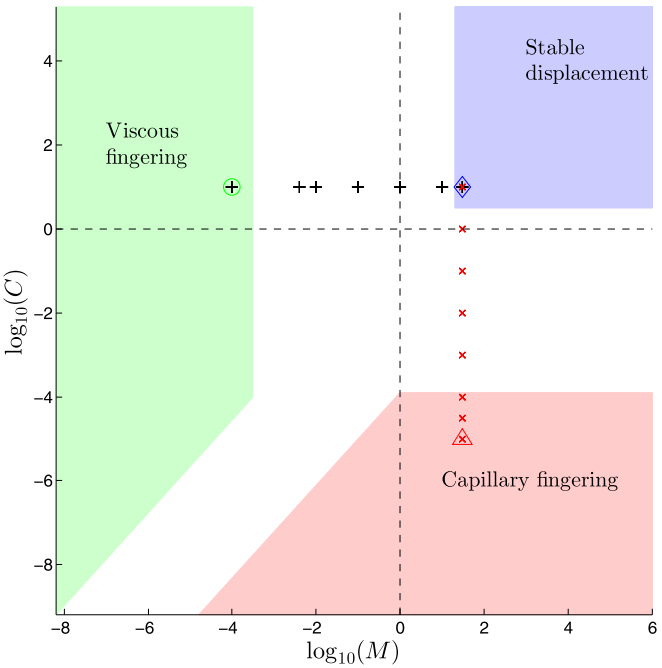

FIG. 12. Lenormand's phase diagram and the CGM simulation parameters corresponding to the "cross" and "plus" symbols. The "circle," "diamond," and "triangle" symbols correspond to parameters where an animation of the simulation is available in the Supplemental Material [94]. Note that the three regime Lenormand plateaus (viscous fingering, stable displacement, and capillary fingering) are illustrated only for qualitative comparison as the exact position of these plateaus depends on many factors [55].

to invade the pores that show the lower capillary resistivity (i.e., the larger one). During capillary fingering, although the advancing front is rather flat, return flow of the nonwetting phase and trapping of the wetting fluid (i.e., blobs formation) must be expected. Average saturation values in between the two previous regimes have to be therefore expected. Thanks to pore-network calculations and laboratory experiments, Lenormand *et al.* show that different experiments conducted in the same region of the phase diagram lead to very similar saturation (i.e., the saturation plateaus in Lenormand's work). However, while moving from one region to others of the phase diagram, either by fixing M and varying C or vice versa, a transition region between three different extremes must be expected where the saturation of the invading phase will monotonously evolve from one plateau value to the other.

c. Random porous network. Although it is not possible to construct with LBM exactly the same random porous networks as in the paper of Lenormand *et al.*, it is still possible to simulate very similar random networks where the same basic flow mechanism should also appear. As in the work of Lenormand *et al.*, our random porous networks are also made of random structured interconnected capillaries. One difference is that the pores and throats are two dimensional here, but in contrast to the various computational approaches taken in Lenormand *et al.* the porous geometry and the multiphase fluid dynamics are fully modeled here. The average radius of the pores and the throats are respectively $\overline{R}_p$ and $\overline{R}_t$. Each pore radius R_p and each throat radius R_t are distributed randomly but uniformly such that $R_p \in [\overline{R}_p - \epsilon_p, \overline{R}_p + \epsilon_p]$ and $R_t \in [\overline{R}_t - \epsilon_t, \overline{R}_t + \epsilon_t]$ respectively. The symbols ϵ_p and ϵ_t stand for the maximum gaps. The distance between the pores is always equal to $D_p = 3\overline{R}_p + \epsilon_p$. On top of that, one throat in five is randomly absent in order to add more randomness. The bottom ($z = 0$) and top ($z = H$) of each random porous media are a no-slip boundary condition. Figure 13 illustrates the geometry of one such random network.

d. Lattice Boltzmann parameters. For simplifying the presentation of this test case, we adopt immediately the lattice unit convention where $\Delta x = \Delta t = 1$. The lengths $L = 980$ and $L_I = L_O = 20$ while the height $H = 980$. The radii $\overline{R}_p = 12$ and $\overline{R}_t = 4$ while the gaps $\epsilon_p = 2$ and $\epsilon_t = 1$. So on the proposed porous domain size of 980×980 lattice sites, the network contains approximately 26×26 pores which is roughly equal to the 25×25 pores network of Lenormand *et al.* As described by Lenormand *et al.*, the inlet fluid has to be nonwetting and so we set $\theta_c = 135^\circ$. The inputs of a simulation are the density ratio $\gamma = \rho_I^0/\rho_O^0$, the kinematic viscosity ratio $q = \nu_I/\nu_O$, and the capillary number C. In our simulations, we set the densities $\rho_I^0 = 1$ and $\rho_O^0 = \rho_I^0/\gamma$. If the kinematic viscosity ratio q is greater than or equal to 1 then the kinematic viscosities $\nu_I = 1/6$ and $\nu_O = \nu_I/q$, otherwise $\nu_O = 1$ and $\nu_I = \nu_O q$. Note that the dynamic viscosity ratio is simply $M = \gamma q$. The inlet velocity $u_I = 0.000\,05$ for most simulations, however, for the lower capillary number, the inlet velocity was reduced down to $u_I = 0.000\,005$. As a consequence $\mathrm{Re} \leqslant 0.02$ for all simulations in this section which is deemed sufficiently small, and it can go as low as $\mathrm{Re} = 0.000\,12$ for the smallest capillary numbers for numerical stability reason.

e. Numerical setup. Since our numerical code is three dimensional, the MRT-D3Q15 model with $\chi = 4/5$ is used in order to reduce the total computational time. To reduce it further, the number of lattice sites in the belt around the block data for MPI communication is equal to 1. This allows us to have only two sites thickness for the two-dimensional domain. Reducing the communication belt to 1 also has the consequence of using only the first neighbors in the nonlocal gradient computation, so 3D fourth-order isotropic discretizations [88] are used on all lattice sites except for the lattice sites in $\mathbf{X}_W$ where a standard 1D first-order forward, first-order backward, and/or second-order centered discrete gradient [89] is used. These gradients are also set to zero on the inlet and outlet boundary lattice sites. The standard full-way bounce back rule is used for all solid lattice sites in $\mathbf{X}_S$. The inlet and outlet fluids are initialized with an equilibrium distribution at zero velocity with the inlet fluid where $x < L_I + 10$ and the outlet fluid elsewhere. The previously described wetting boundary condition in Sec. II E is also applied before the perturbation step. On the inlet and outlet boundaries and as described in Sec. II D, regularized velocity and density boundary conditions are used such that u_I and ρ_O^0 are respectively imposed. Other parameters [77] are $\eta = 0$ and $\beta^* = 0.7$.

f. Evaluation of the saturation S and the stopping criterion. The saturation S of the nonwetting inlet fluid is evaluated exactly as in the Washburn test case. Every 5000 time steps, the saturation S of the porous media is computed as well as the exit saturation S_e along the line of the porous media exit $x = L_I + L$. The simulations are stopped when the exit saturation

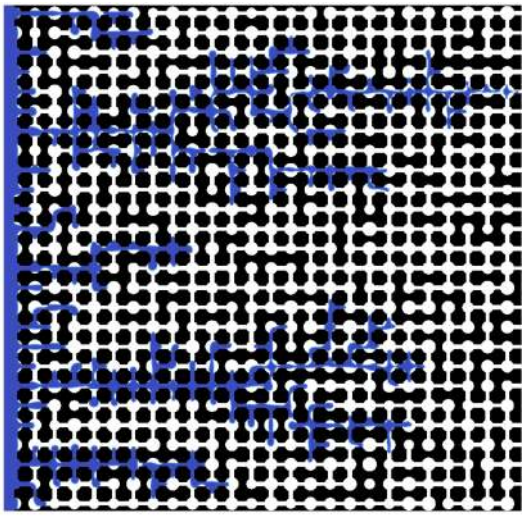

(a)

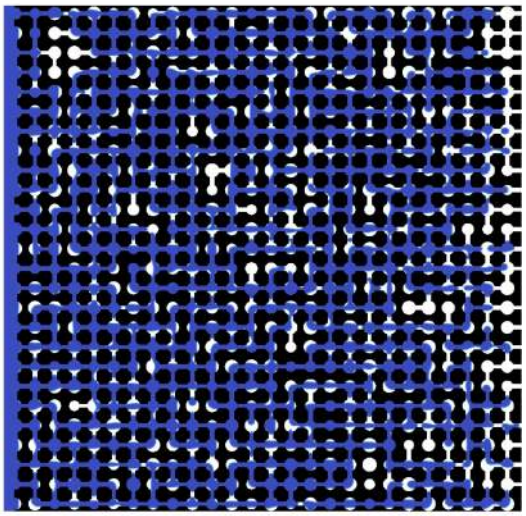

(b)

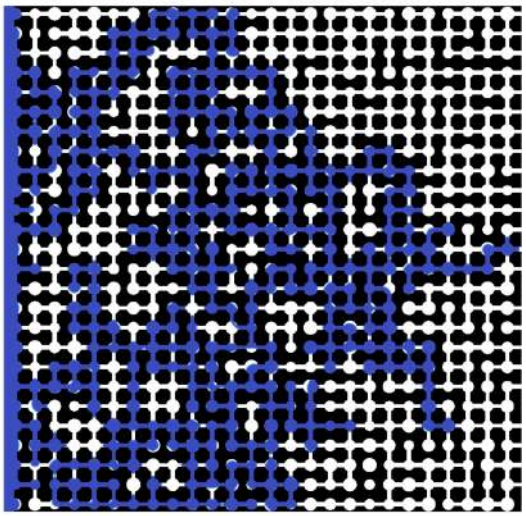

(c)

FIG. 13. Displacement regimes in random porous media: (a) viscous fingering, (b) stable displacement, and (c) capillary fingering. An animation of these simulations is available in the Supplemental Material [94].

S_e is greater than 0.001. In other words, as soon as the inlet fluid reaches the outlet buffer zone, the simulation is stopped.

2. *Discussion of the results*

Immiscible fluids flow solvers that aim to model fluids displacements at the pore scale and successfully recover the different transport regimes as presented by Lenormand *et al.* [55] need to be able to do the following:

(1) deal with important dynamic viscosity ratios between the two immiscible fluids;

(2) deal with varying fluid-solid wetting properties;

(3) implement proper boundary conditions; and

(4) offer the opportunity to play with an important parameter space in order to explore the different region of the phase diagram proposed by Lenormand.

In this section we show that the proposed LB model succeeds in recovering these three different displacing regimes and well reproduces the expected qualitative behavior during the transitions stages where capillary and viscous pressure drops may have comparable magnitudes. Actually, for Fig. 13, animations are available in the Supplemental Material [94] and these clearly show the three different displacement regimes.

As shown in Fig. 12, our calculations follow two straight lines over the Lenormand phase diagram. These two straight lines are intended to explore the three main regions of the phase diagram within the limits of stability of our LB code and are obtained by the following:

(1) keeping a constant capillary number $\log_{10}(C) = 10$, and varying $\log_{10}(M)$ between -4 and 1.48; and

(2) keeping a constant viscosity ratio $\log_{10}(M) = 1.48$, and varying $\log_{10}(C)$ between -5 and 1.

The first line allows us to appreciate the transition between viscous and stable displacement regimes, where viscous

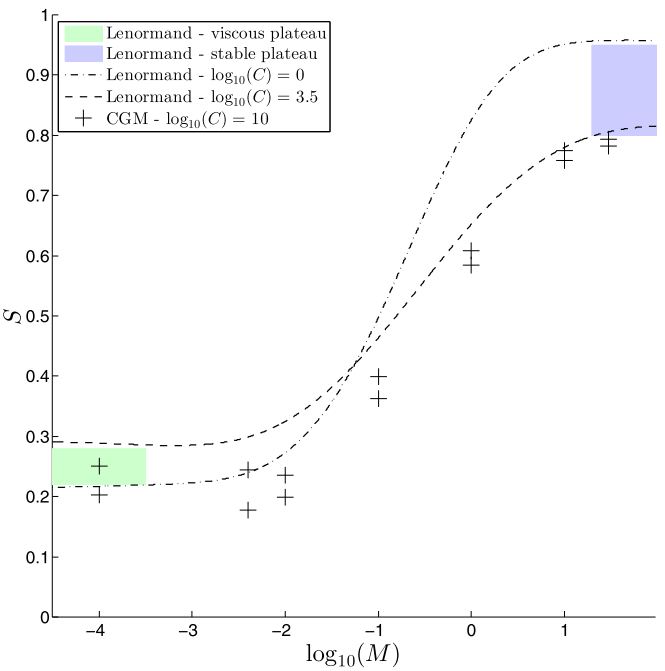

FIG. 14. Saturation S of random porous media as function of the dynamic viscosity ratio M. The jump transition from viscous to stable regime is qualitatively captured by the CGM.

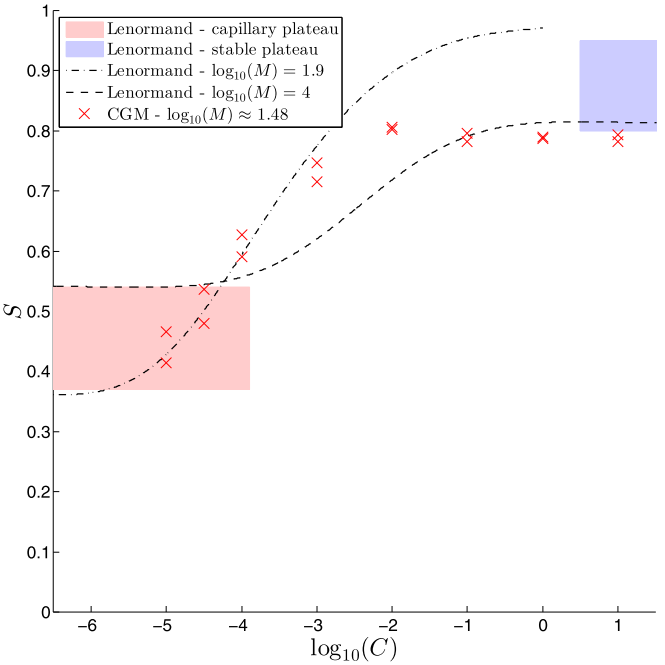

FIG. 15. Saturation S of random porous media as function of the capillary number C. The jump transition from capillary to stable regime is qualitatively captured by the CGM.

pressure drops dominate; see Fig. 14. The second one, on the other hand, investigates how viscous and capillary stresses compete and explore the transition region that separates the stable front displacement and capillary fingering regions; see Fig. 15.

We are confident that our model is stable for an even larger parameter space, but it may require us to lower the Reynolds number, and this is particularly true if the capillary number shall be lower than $\log_{10}(C) = -5$. Unfortunately, the lower the Reynolds number, the longer is the simulation and this becomes computationally prohibitive.

We qualitatively compare our results with the pore-network calculations conducted by Lenormand *et al.*; see dashed lines in Figs. 14 and 15. A quantitative comparison is out of our scope for several reasons. First, we conduct calculations on different but similar porous media geometry. Second, the two models are based on different assumptions; where the lattice Boltzmann method deals with intra-pore-scale processes by resolving the full Navier-Stokes equations, pore network models are based on occupancy rules (i.e., whether or not pore and throats can be invaded) dictated by force balance thresholds. Therefore, in pore-network calculations pores and throats, if invaded, are fully saturated, an approximation that does not apply to LB calculations. Our LB calculations show an excellent qualitative agreement while exploring the two transitional regimes.

In order to show the consistency of the presented lattice Boltzmann model, our calculations are performed on two different, but statistically similar (i.e., similar number of pores and throats and range of throat apertures) randomly generated porous-media geometries. We obtain similar final saturation S for the two sets of runs, results that give us confidence on the quality and reproducibility of our calculations.

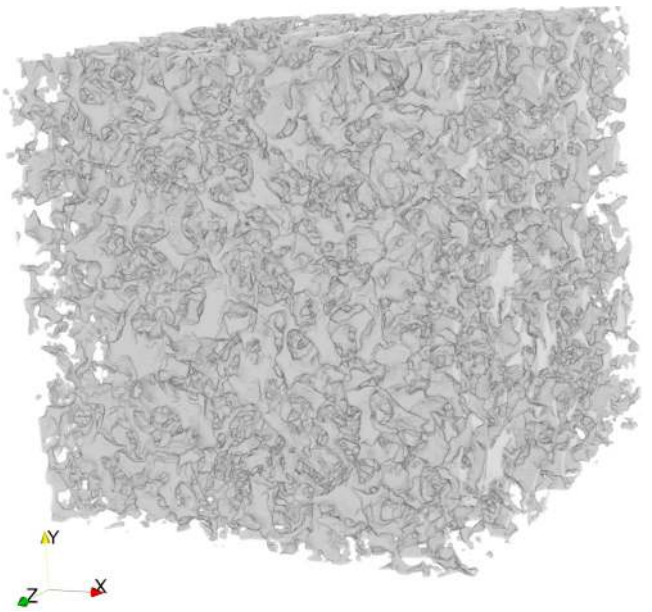

FIG. 16. Pore matrix of the Berea sandstone [85]. The full pore matrix is discretized in a lattice of size $400 \times 400 \times 400$. This corresponds to a resolution of 5.3 μm^3 per voxel.

E. Berea sandstone

1. Physical and numerical description

Continuous physical space. The setting of the Berea sandstone test case is explained below. The domain of interest consists of the three-dimensional box $\mathcal{B}$,

$$\mathcal{B} = \{(x,y,z) \in [0, L + L_I + L_O] \times [0, W] \times [0, H]\}, \quad (85)$$

in which the porous media object $\mathcal{O}$ is immersed into the box $\mathcal{B}$:

$$\mathcal{O} = \mathcal{O}_1 \cap \mathcal{O}_2, \quad (86)$$

$$\mathcal{O}_1 = \{(x,y,z) \in \mathcal{B} : 0 \leqslant z \leqslant H\}, \quad (87)$$

$$\mathcal{O}_2 = \{(x,y,z) \in \mathcal{B} : L_I \leqslant x \leqslant L + L_O\}. \quad (88)$$

This configuration corresponds to a real cubic Berea sandstone sample $\mathcal{O}$ of length L, width $W = L$, and height $H = L$. Two additional fully fluid domains of length $L_I = L_O$ that extend on both ends of the sample serve as numerical buffer zones. The digital image we use for our calculations (see Fig. 16 where the rock pore spaces are represented) is open source and is made available by Dong and co-workers [85,95]. The porosity of the sample is 0.19 [85] and the physical size of each voxel is 5.3 μm^3. In-flow and out-flow boundary conditions are placed respectively at $x = 0$ and $x = L + L_I + L_O$, while periodic boundaries are used for the other spatial directions. Depending on two different experiments that we present (i.e., (1) imbibition and drainage with an imposed fluid velocity and (2) imbibition under the influence of a counterworking pressure gradient), we use different inlet and outlet conditions, notably imposed velocity or flux plus a pressure outlet condition, and pressure boundary conditions applied on both ends of the porous medium. The solid boundaries of the porous

TABLE I. Final total saturation of the intruding fluid in the Berea sandstone sample. The intruding fluid is either nonwetting ($\theta_c = 135°$) or wetting ($\theta_c = 45°$).

Case	M	C	Re	Saturation ($\theta_c = 135°$)	Saturation ($\theta_c = 45°$)
Viscous fingering	0.004	10	0.017 960 7	0.088	0.142
Stable displacement	30	10	0.000 431 1	0.337	0.769
Capillary fingering	30	0.0001	0.000 431 1	0.618	0.590

rock are modeled as no slip using the full-way bounce-back method.

2. *Imbibition and drainage with imposed flux (velocity-inlet and density-outlet boundary conditions)*

a. Parameters and numerical setup. The numerical experiments we present in this section, i.e., 3D imbibition and drainage experiments in digital Berea sandstone, are along the same lines as the one we conducted with a 2D-like random porous network. Indeed we use the same physical dimensionless number definition such as the dynamic viscosity ratios M, the capillary number C and, unless stated otherwise, the same simulation settings are also used. The porous medium geometry is different and changing the geometry involves modifying slightly the definition of the Reynolds number. Indeed, the reference length in its definition is chosen as the average pore size $R = 400 \times 0.000\,015\,36/0.002\,138 \approx 2.87$ in lattice units [85]. We, moreover, set an inlet velocity $u_I = 0.000\,025$ for all experiments, with the invading fluid initially fully occupying $x < L_I + 1$ and placing the defending fluid elsewhere, when possible second order gradient discretization is used near the boundary.

Due to the large numerical load of the Berea calculations, i.e., the digital image of the Berea sample is 400^3 lattice units, we limit our analysis only at qualitatively comparing different simulation results obtained for drainage and imbibition scenarios. We performed only a few experiments as shown in Table I.

In the case of drainage, we set the intruding fluid as nonwetting and we chose a static contact angle equal to $\theta_c = 135°$, while for imbibition, where the intruding fluid is wetting, we chose $\theta_c = 45°$. Once the invading fluid reaches the sample exit, we extract the total saturation of the invading fluid (i.e., integrated over the total volume of the sample) and also the saturation along the x axis, [i.e., integration over planes along the normalized stone depth $x^* = (x - L_I)/L$, and that we call here after saturation depth profile]. We underline that when the setup with a velocity-inlet boundary condition (BC) and a nonwetting intruding fluid is used, the pressure at the inlet will necessarily build over time and ultimately overcome the resistive capillary pressure. Consequently the intruding nonwetting fluid will, at some point, reach the outlet buffer zone, ending the simulation.

In Table I we report the results concerning the final total saturation for each regime we simulated.

b. Discussion of the results: Viscous fingering. The final saturation for the drainage viscous fingering regime calculation conducted in the 3D Berea sample is much lower (about twice as much) when compared to the 2D-like one presented above. Since in the viscous regime the invading fluid tends to form preferentially tubelike fingers, we attribute the main reason for the observed discrepancy between 2D-like and 3D calculations to the fact that two-dimensional fingers occupy a physically larger spatial ratio than their three-dimensional counterparts. Moreover, the Berea sample being the digital image of a real rock, it could display a higher degree of heterogeneity.

Although the invasion pattern is clearly viscous fingering dominated, we can notice that the final saturation in imbibition ($S = 0.142$) is significantly larger than with drainage ($S = 0.088$). This is an expected result; indeed in imbibition the invading fingers are expected to be broader [96–98], since they have the tendency to wet the pores and thus explore more easily neighboring pores. Figure 17 shows depth saturation profiles for both imbibition and drainage experiments in the viscous fingering regime. We see that along the stone depth x^*, the imbibition saturation curve is predominantly higher than the drainage saturation one. Figure 18 shows the final views of a drainage simulation (lattice size of $440 \times 400 \times 400$) in the viscous fingering regime. The main invading finger is clearly visible. An animation of this simulation for a reduced size matrix is available in the Supplemental Material [94] (lattice size of $220 \times 200 \times 200$). Figure 19 shows analog results as in Fig. 18 but this time for an imbibition case. Also for this scenario we supply an animation of this simulation for a

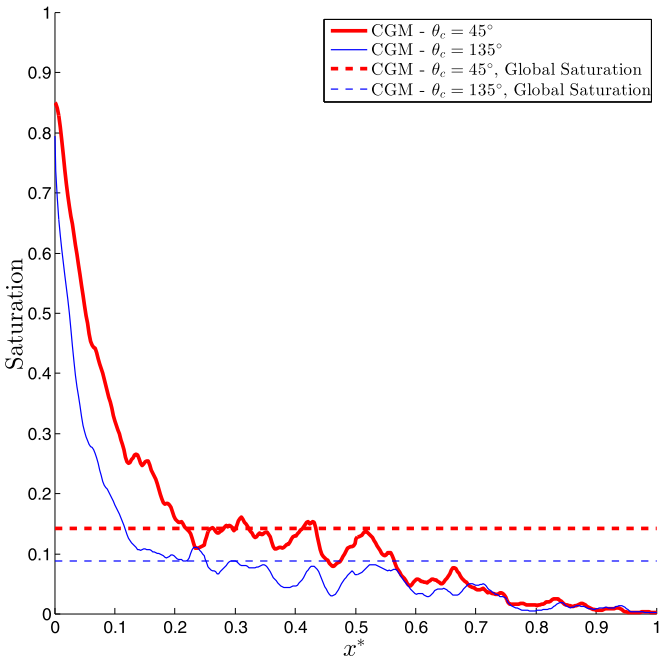

FIG. 17. Saturation of the Berea sandstone as function of the stone depth x^* in the viscous fingering regime. Imbibition ($\theta_c = 45°$) and drainage ($\theta_c = 135°$) are illustrated as well as the corresponding final global saturation of the sample.

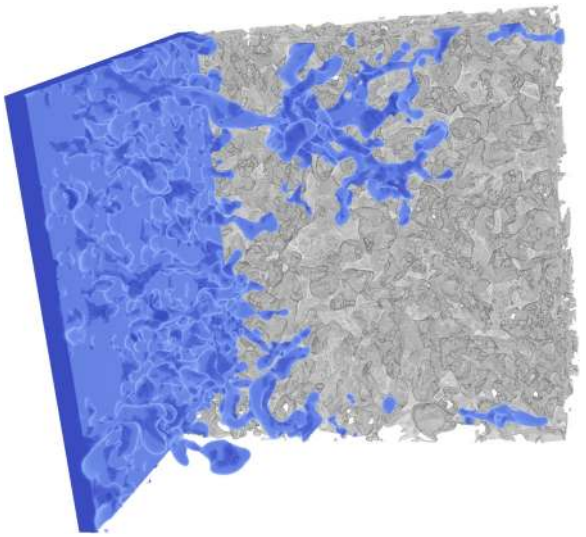

FIG. 18. Final view of a drainage CGM simulation in the viscous fingering regime with half the solid Berea sandstone matrix in the back. An animation of this simulation for a reduced size matrix is available in the Supplemental Material [94].

reduced size matrix in the Supplemental Material [94] (lattice size of $220 \times 200 \times 200$). When comparing Figs. 18 and 19 we clearly see that the bulk region explored by the invading fluid during imbibition and drainage experiments is essentially the same, clearly indicating that the invasion dynamics throughout the whole numerical domain is essentially dominated by viscous pressure drop. However, we can observe that fingers in the imbibition scenario are broader and this is because the favorable wettability of the sample during imbibition favors lateral invasion (i.e., pore-scale processes, overall, are capillary dominated). Figures 18 and 19, show, as the animations

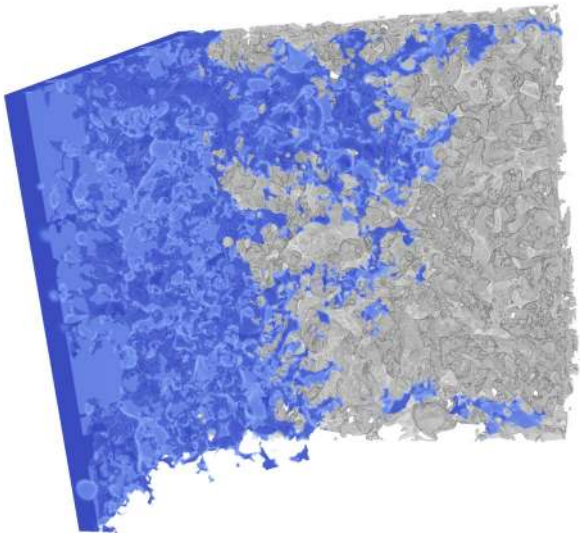

FIG. 19. Final view of an imbibition CGM simulation in the viscous fingering regime with half the solid Berea sandstone matrix in the back. An animation of this simulation for a reduced size matrix is available in the Supplemental Material [94].

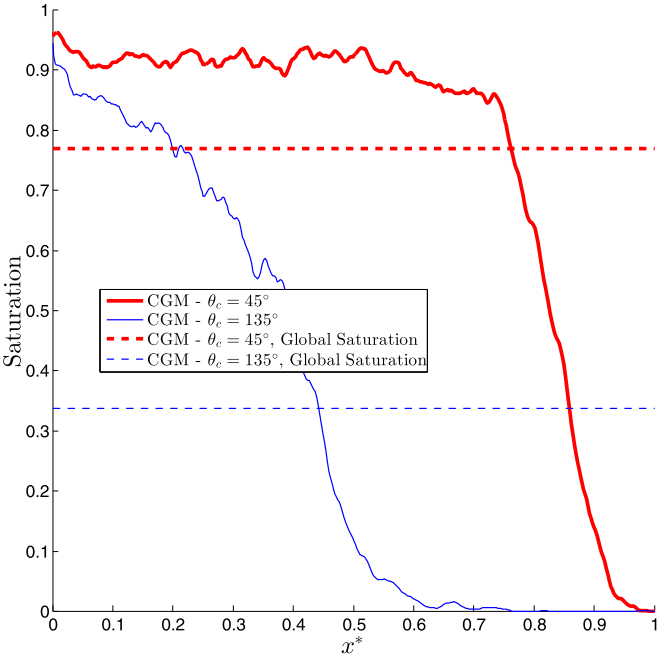

FIG. 20. Saturation of the Berea sandstone as function of the stone depth x^* in the stable displacement regime. Imbibition ($\theta_c = 45°$) and drainage ($\theta_c = 135°$) are illustrated as well as the corresponding final global saturation of the sample.

corroborate visually, that the saturation curve as a function of the stone depth is higher with imbibition than with drainage.

c. Discussion of the results: Stable displacement. In the stable displacement regime, we find a strongly different final saturation between imbibition ($S = 0.769$) and drainage ($S = 0.337$) experiments. This result was unexpected, but a careful analysis of the simulation results reveals why this occurred. Figure 20 shows the saturation depth profiles for imbibition and drainage experiments for the stable displacement regime; saturation depth profiles are sensibly different. In particular, for the drainage case, the second half of the Berea sample seems to be almost unexplored. This is an effect of the fluid-fluid interface dynamics. Indeed, in the drainage situation, isolated droplets can snap off from the main advancing front, as shown in Fig. 21, and move under the push of the displaced wetting fluid, i.e., which is displaced by the pistonlike effect of the advancing stable nonwetting fluid front [99]; the smallest drops (i.e., microdroplets, with a radius sensibly smaller than average pore size and smaller but similar to the throat size) can be scarcely sensible to the capillary resistance of the medium and reach the outlet much earlier than the stable nonwetting front. This situation is much less likely with imbibition because isolated droplets are most likely slowed down and/or trapped by the surrounding nonwetting fluid, which is resistive to displacement. In order to show the presence of single advancing drops, in Fig. 21 we report the logarithm of the saturation depth profile for the drainage case. Here we can clearly see saturation "bumps" in the second half of the porous medium that we attribute to isolate nonwetting droplets. In Fig. 22 we show the final snapshot of the drainage simulation where we can see an isolated droplet that has reached the sample outlet before the main advancing front (black circle).

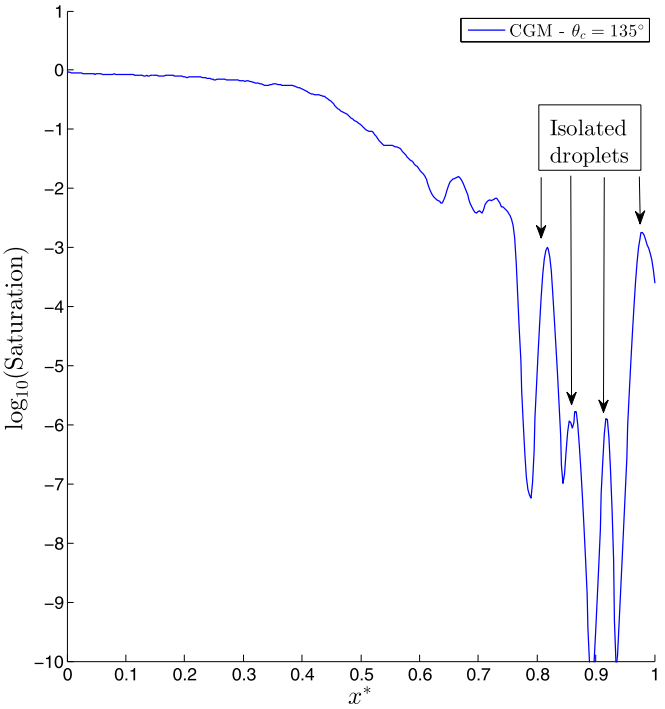

FIG. 21. Logarithm of the saturation of the Berea sandstone as function of the stone depth x^* in the stable displacement regime and drainage ($\theta_c = 135°$).

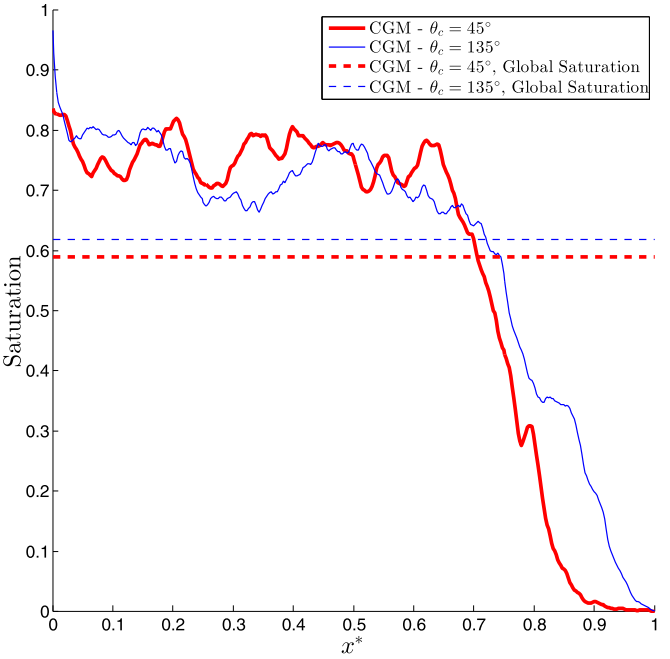

FIG. 23. Saturation of the Berea sandstone as function of the stone depth x^* in the capillary fingering regime. Imbibition ($\theta_c = 45°$) and drainage ($\theta_c = 135°$) are illustrated as well as the corresponding final global saturation of the sample.

So the analysis in the stable displacement regime cannot be based solely on the study of final sample saturation since the effect of the flows on the interface dynamics cannot be ignored even if the Reynolds number is very low ($\approx 0.000\,431\,1$ here). In the stable displacement regime coupled with a drainage situation, the interfacial tension can be really small and the flows can still drive isolated droplets into the center of the pores and move faster than the main advancing front.

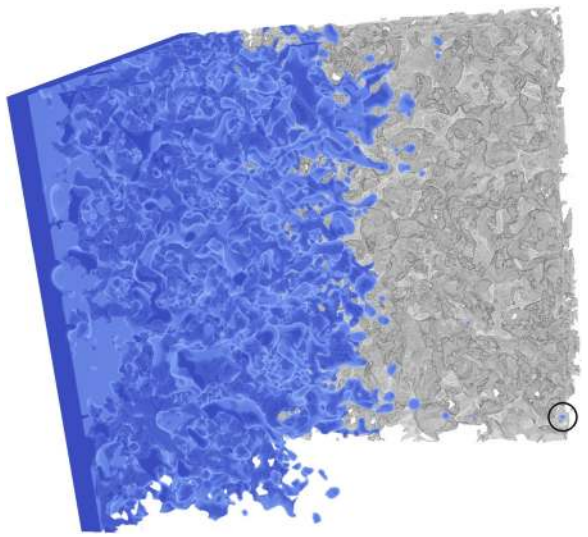

FIG. 22. Final view of a drainage CGM simulation in the stable displacement regime with half the solid Berea sandstone matrix in the back (lattice size of $440 \times 400 \times 400$). It is possible to see in the black circle the isolated droplet that has reached the sample outlet before the main advancing front.

d. Discussion of the results: Capillary fingering. In the capillary fingering regime, the final saturation is very similar to imbibition ($S = 0.590$) and drainage ($S = 0.618$) experiments. Figure 23 shows saturation depth profiles for both imbibition and drainage calculations. It is reasonable to assume that the net flow effects on the interface dynamics are much less important in the capillary fingering regime than in the stable displacement regime since the interfacial tension is much higher. One may also remark that the imbibition filling process seems to explore further the beginning than the end of the sample compared to the drainage scenario. However, the differences in the saturation curves are rather small and this makes it difficult to make a clear analysis. Indeed, the difference between imbibition and drainage final saturation was about 100% for the viscous fingering and stable displacement regime. An explanation was clearly needed in these cases. So overall, it is difficult to tackle the task of explaining these small differences. We rather say that in our specific cases the difference between imbibition and drainage in the resulting dynamics of capillary fingering appears to be small and that we could not find any distinct significative phenomena for these simulated parameters. Note that this does not imply that there are no distinct phenomena.

3. Imbibition under the influence of a counterworking pressure gradient (density-inlet and density-outlet BCs)

In this experiment we are interested in testing our model in the case where the naturally advancing front of a wetting fluid (i.e., under the positive effect of capillary forces) is slowed down or stopped by a counterworking pressure gradient. For

instance, our goal is to find the critical pressure difference to apply at the outlet for which the overall flow is stopped. This setup is of interest for environmental engineering applications, where engineered changes in hydraulic heads may be used to inhibit the advancing front of DNAPL contamination events [100]. Moreover this experiment gives us the opportunity to show the superiority of the wetting BC we propose with respect to the standard one and test the regularized BC in the case where both ends of the porous medium are subject to pressure boundary conditions.

a. Dimensionless quantities. The dimensionless numbers used to describe this physical problem are different than with a velocity inlet. Instead of the capillary and Reynolds number which are well defined with a reference velocity, the following dimensionless numbers are carefully chosen:

$$\mathrm{La} = \frac{\sigma R_t \rho_I^0}{\mu_I^2}, \tag{89}$$

$$\mathcal{L} = \frac{1}{2}\frac{\Delta P R_t}{\sigma \cos(\theta_c)}, \tag{90}$$

where $R_t = 200 \times 0.000\,040\,06/0.002\,138 \approx 3.74$ is the maximum throat radius [85] of the sample in a lattice unit and ΔP is the pressure variation across the sample, with the pressure being higher at the outlet than at the inlet so the flow can be stopped. The first dimensionless number is the well-known Laplace number La which relates the capillaries to the viscous forces. The second one was derived from the Laplace-Young law across a tube of radius R_t when the capillary pressure ΔP_c is equal to the pressure difference ΔP along the tube. This is the simplest case where a situation of no flow appears. If this idea is extended to a core sample ideally represented by many tubes in parallel, the flow will not pass through the principal and largest tube of radius R_t if $\mathcal{L} = 1$. Of course, the flow would still pass through the smaller capillaries, but by Washburn law, when the throat radius gets smaller the penetration velocity also gets smaller. So the fluid penetration in the smaller capillaries evolve according to a much larger time scale and a much lower spatial scale than the larger capillaries. That is the reason for choosing the maximum throat radius R_t of the sample as the reference length. If the many tubes in parallel assumption is not too far-fetched for some complex porous media, we would therefore expect that the critical permeable-impermeable threshold would be around $\mathcal{L} = 1$ *for the larger capillaries and for the shorter time scale*. Smaller capillaries as well as the complex geometry shape may still play an important role, so it would not be surprising that the critical permeable-impermeable threshold $\mathcal{L}$ might be larger or lower than 1, but a value around $\mathcal{L} = 1$ is a good initial guess. At the very least, the larger the dimensionless quantity $\mathcal{L}$, the more difficult it becomes for the intruding flow to cross the sample in a reasonable amount of time. Inversely, the smaller $\mathcal{L}$, the easier it gets for the intruding fluid to pass through the main path. For these simulations, we used a unit density ratio, a viscosity ratio of $M = 30$, a contact angle of $\theta_c = 45^\circ$, and $\mathrm{La} = 2$. The value of the Laplace number was chosen such that the interfacial tension force is high compared to the viscous force and as a consequence, the time scale for which the physical imbibition phenomenon appears is short.

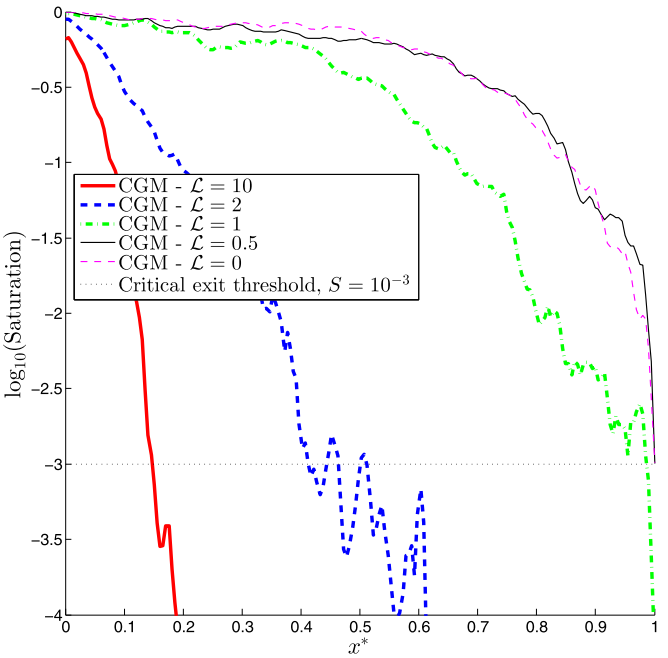

FIG. 24. Saturation of the Berea sandstone as function of the stone depth x^* and the dimensionless quantity $\mathcal{L}$. The critical exit saturation threshold for percolation is also illustrated. Only the cases with $\mathcal{L} = 0$ and $\mathcal{L} = 0.5$ percolate the core sample under the chosen steady state simulation criterion.

b. Steady-state consideration. Since the computation in this section involves steady state flows and these are rather expensive to compute with the lattice Boltzmann method, we decided to reduce the resolution of the Berea sandstone by a factor of 2 in each dimension using the algorithm in Ref. [101]. With a lower resolution of the core sample only the larger space and shorter time scale of the main flow are captured (which also follow the idea above of using $\mathcal{L}$ as a representative dimensionless quantity). The stopping criterion of the simulations is one of the following:

(1) a steady state is reached when the relative global saturation difference in a time window of 5000 time steps is less than 10^{-4}, in which case the sample is then considered as impermeable;

(2) when the saturation along the sample exit plane is more than 10^{-3}, in which case the sample is then considered as permeable.

Note that the saturation is measured as in the previous test case.

c. Discussion of the results. Figure 24 shows the depth saturation profiles as function of the dimensionless quantity $\mathcal{L}$. Only the cases with $\mathcal{L} = 0$ and $\mathcal{L} = 0.5$ percolate the core sample under the chosen steady state simulation criterion. The case with $\mathcal{L} = 1$ nearly percolates the sample. It is clear that a more conservative stopping criterion would have led to percolation in that case. Overall, this test illustrates that the estimation of percolation near $\mathcal{L} = 1$ seems to be a good initial guess in order to find the critical percolation threshold. As stated above, a high $\mathcal{L}$ number indicates that it is difficult to percolate the sample (on the larger space and shorter time scale). Figure 25 shows the global saturation of the Berea

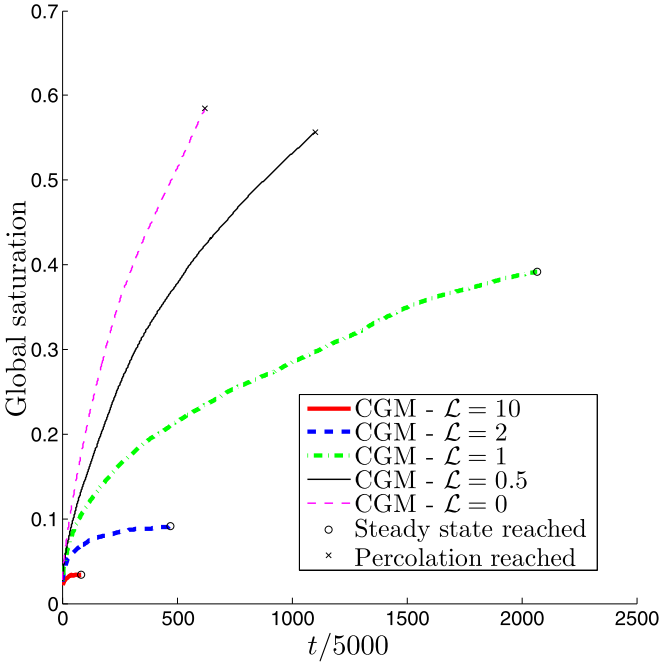

FIG. 25. Global saturation of the Berea sandstone as function of the time (in lattice units) and the dimensionless quantity $\mathcal{L}$.

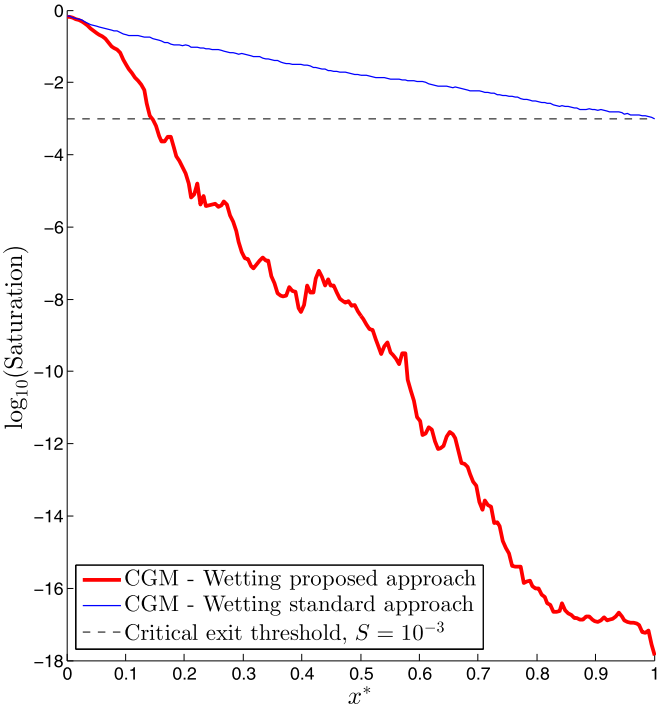

FIG. 26. Saturation of the Berea sandstone as function of the stone depth x^* and the type of wetting boundary conditions. The dimensionless quantity $\mathcal{L} = 10$ which means that there is a strong inverse pressure gradient. The standard wetting boundary conditions do not behave as expected with such a strong inverse pressure gradient.

sandstone as function of the time (in lattice units) and the dimensionless quantity $\mathcal{L}$. We see that percolation cannot be reached in the shorter time scale if $\mathcal{L}$ is high enough which is in accordance with the theory and analysis advanced above. Indeed, the global saturation rapidly reach a level for which it will not be possible to percolate the sample in a reasonable amount of physical time (that can be tackled with a simulation). The case with $\mathcal{L} = 0$ percolates the sample and this is in accordance with the many tubes in parallel geometrical approximation of porous media described above, i.e., the percolation is held to happen and much faster than with a high $\mathcal{L}$ number.

d. Note on standard wetting boundary condition. We would like to note that the development of this numerical method was mainly done in order to fill the need to simulate with more accuracy the imbibition process in porous media. Indeed, the widely used and standard wetting boundary condition for the multiphase lattice Boltzmann method is not adequate to simulate wetting phenomena. This was clearly shown in a previous publication on simple test case [44]. This is shown again in Fig. 26 which presents the saturation of the Berea sandstone as function of the stone depth x^* and the proposed versus the standard wetting boundary conditions. The dimensionless number $\mathcal{L} = 10$ is used in these simulations and this means that a very strong inverse pressure gradient is imposed. It required 285 000 time steps to percolate the sample with the standard wetting boundary condition while 420 000 time steps were needed to reach steady state with the proposed wetting boundary condition. The difference in behavior of the numerical method is huge! From our theoretical consideration above, with $\mathcal{L} = 10$, it makes much more physical sense to achieve a nonpercolating steady state. Indeed, the standard wetting boundary condition is incorrect and this is because there is an uncontrollable numerical mass transfer along the solid boundary of the porous media. It is clear that we could not do all the above scientific analysis to numerically study wetting phenomena while using the standard approach. So overall, we strongly welcome and suggest using the proposed wetting boundary condition to simulate the imbibition process in porous media with LBM.

IV. CONCLUSION

This article proposes an extension of a 2D CGM to 3D simulations with the D3Q15, D3Q19, and D3Q27 lattices. The model is provided with sufficient detail to allow it to be easily reproduced by the reader; matrices, stencils, weights, and indexes can be found in the Appendix. This work also significantly contributes to the advancement of the computational modeling of multiphase or multicomponent fluid flows under the influence of wetting properties with the lattice Boltzmann technique and, more in particular, with the CGM, extending its range of applicability in porous-media applications. To improve the numerical model, we extended the three-dimensional regularized velocity and density boundary conditions to CGM, which allowed us to easily specify in-flow and out-flow boundaries for fluids characterized by different densities. Moreover, we proposed a three-dimensional wetting boundary condition which we rigorously validated for both variable density and viscosity ratios, within values typical for liquid-liquid compounds. To validate the method, we have shown that Jurin's and Washburn's laws, which both depend on a proper model for fluid-fluid and fluid-solid interfacial tension

properties, are well captured by the proposed numerical approach. Moreover, to extend the many existing validations attempted with the CGM, we have also demonstrated that the CGM is capable of modeling three-dimensional capillary waves for a wide range of liquid-liquid density and viscosity ratios. Furthermore, by using simple 2D-like random porous networks, we were able to show that the proposed CGM, in conjunction with the regularized inlet, outlet and proposed wetting boundary conditions, is able to qualitatively reproduce the various imbibition regimes (i.e., viscous fingering, stable displacement, and capillary fingering) and the associated transition zones as classified by Lenormand.

Finally, in order to explore the capabilities of CGM for realistic engineering scenarios, we performed 3D imbibition and drainage experiments in a digitalized Berea sandstone and reproduced the three main fluid invasion regimes. We demonstrated that the proposed wetting boundary condition is more suitable for simulating imbibition in porous media than the LBM standard wetting boundary approach. This is, in our opinion, the principal advantage of our proposed method, along with the ability to describe flows with variable density ratios more accurately in a range of values of high interest in many industrial areas, including the oil industry and DNAPL decontamination processes. We would also like to point out that wetting properties can easily be locally adjusted in our model. Therefore, nothing prevents our model from being applied, in the future, to applications where spatially variable wetting properties are needed, such as microfluidics applications [102] and porous rocks characterized by strongly variable mineral assemblies [103]. We finally would like to highlight that our code was implemented and added to the well-established LBM open-source PALABOS library [68] and that we intend to make our code available to the public under the same license; a choice that we strongly believe will further stimulate the industries and the academics to advance the use of LB codes for both industrial and research applications in the field of pore scale of multiphase or multicomponent flows in porous media.

ACKNOWLEDGMENTS

S.L. thanks the FRQNT "Fonds de recherche du Québec—Nature et technologies" for financial support (Research Scholarship No. 183583). We also thank the Center for Advanced Modeling Science CADMOS for financial support and computational resources. A.P. would further like to thank the Swiss National Science Foundation SNF for financial support (Ambizione Grant No. 154854) and the Swiss National Supercomputing Center CSCS for computational resources (Project No. s597).

APPENDIX

The Appendix is organized in two sections:

(1) the theoretical derivation of the lattice weights for CGM; and

(2) the MRT matrices.

1. Derivation of the lattice weights for CGM

In the equilibrium distribution of Eq. (4), the weights W_i are already known and are the standard lattice weights of the

TABLE II. D2Q9 lattice velocity and weights.

D2Q9	$\{i : \lvert\mathbf{c}_i\rvert^2 = 0\}$	$\{i : \lvert\mathbf{c}_i\rvert^2 = 1\}$	$\{i : \lvert\mathbf{c}_i\rvert^2 = 2\}$
W_i	4/9	1/9	1/36
ϕ_i	0	1/5	1/20
φ_i	1	−1/5	−1/20
ψ_i	−8/3	−1/6	1/12
ξ_i	0	1/2	1/8
B_i	−4/27	2/27	5/108
$\mathbf{c}_i$	$\mathbf{c}_0 = (0,0)$	$\mathbf{c}_2 = (-1,0)$ $\mathbf{c}_4 = (0,-1)$ $\mathbf{c}_6 = (1,0)$ $\mathbf{c}_8 = (0,1)$	$\mathbf{c}_1 = (-1,1)$ $\mathbf{c}_3 = (-1,-1)$ $\mathbf{c}_5 = (1,-1)$ $\mathbf{c}_7 = (1,1)$

TABLE III. D3Q15 lattice velocity and weights.

D3Q15	$\{i : \lvert\mathbf{c}_i\rvert^2 = 0\}$	$\{i : \lvert\mathbf{c}_i\rvert^2 = 1\}$	$\{i : \lvert\mathbf{c}_i\rvert^2 = 3\}$
W_i	2/9	1/9	1/72
ϕ_i	0	1/7	1/56
φ_i	1	−1/7	−1/56
ψ_i	−5/3	−1/3	1/12
ξ_i	0	1/2	1/16
B_i	−4/27	1/27	7/216
$\mathbf{c}_i$	$\mathbf{c}_0 = (0,0,0)$	$\mathbf{c}_1 = (-1,0,0)$ $\mathbf{c}_2 = (0,-1,0)$ $\mathbf{c}_3 = (0,0,-1)$ $\mathbf{c}_8 = (1,0,0)$ $\mathbf{c}_9 = (0,1,0)$ $\mathbf{c}_{10} = (0,0,1)$	$\mathbf{c}_4 = (-1,-1,-1)$ $\mathbf{c}_5 = (-1,-1,1)$ $\mathbf{c}_6 = (-1,1,-1)$ $\mathbf{c}_7 = (-1,1,1)$ $\mathbf{c}_{11} = (1,1,1)$ $\mathbf{c}_{12} = (1,1,-1)$ $\mathbf{c}_{13} = (1,-1,1)$ $\mathbf{c}_{14} = (1,-1,-1)$

TABLE IV. D3Q19 lattice velocity and weights.

D3Q19	$\{i : \lvert\mathbf{c}_i\rvert^2 = 0\}$	$\{i : \lvert\mathbf{c}_i\rvert^2 = 1\}$	$\{i : \lvert\mathbf{c}_i\rvert^2 = 2\}$
W_i	1/3	1/18	1/36
ϕ_i	0	1/12	1/24
φ_i	1	−1/12	−1/24
ψ_i	−5/2	−1/6	1/24
ξ_i	0	1/4	1/8
B_i	−2/9	1/54	1/27
$\mathbf{c}_i$	$\mathbf{c}_0 = (0,0,0)$	$\mathbf{c}_1 = (-1,0,0)$ $\mathbf{c}_2 = (0,-1,0)$ $\mathbf{c}_3 = (0,0,-1)$ $\mathbf{c}_{10} = (1,0,0)$ $\mathbf{c}_{11} = (0,1,0)$ $\mathbf{c}_{12} = (0,0,1)$	$\mathbf{c}_4 = (-1,-1,0)$ $\mathbf{c}_5 = (-1,1,0)$ $\mathbf{c}_6 = (-1,0,-1)$ $\mathbf{c}_7 = (-1,0,1)$ $\mathbf{c}_8 = (0,-1,-1)$ $\mathbf{c}_9 = (0,-1,1)$ $\mathbf{c}_{13} = (1,1,0)$ $\mathbf{c}_{14} = (1,-1,0)$ $\mathbf{c}_{15} = (1,0,1)$ $\mathbf{c}_{16} = (1,0,-1)$ $\mathbf{c}_{17} = (0,1,1)$ $\mathbf{c}_{18} = (0,1,-1)$

TABLE V. D3Q27 lattice velocity and weights.

D3Q27	$\{i : \lvert\mathbf{c}_i\rvert^2 = 0\}$	$\{i : \lvert\mathbf{c}_i\rvert^2 = 1\}$	$\{i : \lvert\mathbf{c}_i\rvert^2 = 2\}$	$\{i : \lvert\mathbf{c}_i\rvert^2 = 3\}$
W_i	8/27	2/27	1/54	1/216
ϕ_i	0	2/19	1/38	1/152
φ_i	1	−2/19	−1/38	−1/152
ψ_i	−20/9	−2/9	1/36	1/36
ξ_i	0	1/3	1/12	1/48
B_i	−16/81	2/81	2/81	7/648
$\mathbf{c}_i$	$\mathbf{c}_0 = (0,0,0)$	$\mathbf{c}_1 = (-1,0,0)$ $\mathbf{c}_2 = (0,-1,0)$ $\mathbf{c}_3 = (0,0,-1)$ $\mathbf{c}_{14} = (1,0,0)$ $\mathbf{c}_{15} = (0,1,0)$ $\mathbf{c}_{16} = (0,0,1)$	$\mathbf{c}_4 = (-1,-1,0)$ $\mathbf{c}_5 = (-1,1,0)$ $\mathbf{c}_6 = (-1,0,-1)$ $\mathbf{c}_7 = (-1,0,1)$ $\mathbf{c}_8 = (0,-1,-1)$ $\mathbf{c}_9 = (0,-1,1)$ $\mathbf{c}_{17} = (1,1,0)$ $\mathbf{c}_{18} = (1,-1,0)$ $\mathbf{c}_{19} = (1,0,1)$ $\mathbf{c}_{20} = (1,0,-1)$ $\mathbf{c}_{21} = (0,1,1)$ $\mathbf{c}_{22} = (0,1,-1)$	$\mathbf{c}_{10} = (-1,-1,-1)$ $\mathbf{c}_{11} = (-1,-1,1)$ $\mathbf{c}_{12} = (-1,1,-1)$ $\mathbf{c}_{13} = (-1,1,1)$ $\mathbf{c}_{23} = (1,1,1)$ $\mathbf{c}_{24} = (1,1,-1)$ $\mathbf{c}_{25} = (1,-1,1)$ $\mathbf{c}_{26} = (1,-1,-1)$

lattice Boltzmann method [69]. The derivation of the weights is ϕ_i, φ_i, ψ_i, ξ_i, and ζ for the two- and three-dimensional lattices. The methodology is based on a Chapman-Enskog analysis from Refs. [37,78] which the latter states that with variable density, the equilibrium distribution functions should satisfy slightly different constraints than in the case of a single-phase flow with near constant density. Those methodologies were adapted in Ref. [39] for the color-blind distribution functions of the color-gradient multiphase D2Q9 model. Below, we described a more general methodology to extract valid weights on two- or three-dimensional lattices.

First, the speed of sound weight ζ in Eq. (11) is chosen such that if the free parameters $\alpha_k = W_0$, then the square of the isothermal speed of sound will be equal to 1/3 as is usually the case in the standard single-phase lattice Boltzmann method. Then, the weights ϕ_i and φ_i are determined following the principle of mass conservation, momentum conservation, momentum flux tensor, and constitutive physics of a single-phase lattice Boltzmann method [78]. To take into account variable density of a multiphase flow, the weights ψ_i and ξ_i must be carefully chosen and the constraints on the color-blind distribution functions are

$$\sum_i N_i^{(e)} = \rho, \tag{A1}$$

$$\sum_i N_i^{(e)} c_{i,m} = \rho u_m, \tag{A2}$$

$$\sum_i N_i^{(e)} c_{i,m} c_{i,n} = +P_{mn} + \rho u_m u_n + \overline{\nu}[u_m \partial_n(\rho) + u_n \partial_m(\rho) + u_o \partial_o(\rho)\delta_{mn}], \tag{A3}$$

$$\sum_i N_i^{(e)} c_{i,m} c_{i,n} c_{i,o} = \frac{\rho}{3}(u_m \delta_{no} + u_n \delta_{mo} + u_o \delta_{mn}), \tag{A4}$$

where (m,n,o,p) is the index notation, δ is the Kronecker function, and $P_{mn} = \sum_k P_{mn}^k$ is the color-blind pressure tensor. These relations make sure that the macroscopic equations are respected in the single-phase region while an interpolation is applied at the interface for the viscosity $\overline{\nu}$ and the color-blind P_{mn} pressure tensor.

Under these constraints, ψ_i and ξ_i are now the only unknowns left in a system of equations (A1)–(A4) with more unknowns than constraints. So, there is still some degree of freedom within the system and to close the system of equations, we proposed to minimize the following functional using the method of Lagrange multiplier:

$$\sum_i \frac{\{\overline{\nu}[\psi_i(\mathbf{u}\cdot\nabla\rho) + \xi_i(\mathbf{G} : \mathbf{c}_i \otimes \mathbf{c}_i)]\}^2}{W_i}. \tag{A5}$$

This functional, weighted by the standard lattice weights W_i, has the goal to minimize the difference with the single-phase flow equilibrium distribution. Once solved, the weights ψ_i and ξ_i are found.

The last weights B_i are related to the capillary stress tensor and are derived in a similar fashion as in Refs. [35,43]. We follow the constraints of conservation of mass, momentum,

TABLE VI. Weight ζ related to the isothermal speed of sound $(c_s^k)^2$.

	D2Q9	D3Q15	D3Q19	D3Q27
ζ	$\frac{3}{5}$	$\frac{3}{7}$	$\frac{1}{2}$	$\frac{9}{19}$

TABLE VII. Velocity space indexes $\mathbf{p}$ related to the momentum.

	D2Q9	D3Q15	D3Q19	D3Q27
p_x	3	3	3	1
p_y	5	5	5	2
p_z		7	7	3

and macroscopic form of the capillary stress tensor:

$$\sum_i \left(\Delta N_i^{\text{pert}}\right) = 0, \tag{A6}$$

$$\sum_i \left(\Delta N_i^{\text{pert}}\right)\mathbf{c}_i = 0, \tag{A7}$$

$$\frac{1}{\omega_{\text{eff}}}\sum_i \left(\Delta N_i^{\text{pert}}\right)\mathbf{c}_i \otimes \mathbf{c}_i = \frac{2}{9}\frac{A}{\omega_{\text{eff}}|\mathbf{F}|}(|\mathbf{F}|^2\mathbf{I} - \mathbf{F}\otimes\mathbf{F}), \tag{A8}$$

where $\mathbf{I}$ is the identity tensor and N_i^{pert} is defined as in Eq. (16).

By imposing these constraints on the perturbation weights B_i, the system of equations also has more unknown than equations. To close the system, we again proposed to minimize the following functional using the method of Lagrange multiplier:

$$\sum_i \frac{\left(\Delta N_i^{\text{pert}}\right)^2}{W_i}. \tag{A9}$$

This functional, again weighted by the standard lattice weights W_i, has the goal to minimize the impact of the perturbation operator in the density distribution space.

All the resulting weights needed to complete the numerical scheme are given in Tables II–VI for each lattice. Useful indexes corresponding to the momentum and kinematic viscosity are also respectively given in Tables VII and VIII.

2. MRT matrices

For convenience, the MRT matrices for the D2Q9, D3Q15, D3Q19, and D3Q27 are all consolidated in Tables IX–XII and they follow the lattice connectivity given in Tables II–V.

TABLE VIII. Velocity space indexes υ related to the kinematic viscosity.

	D2Q9	D3Q15	D3Q19	D3Q27
υ	$\{i : i = 7,8\}$	$\{i : i = 9,10,11,12,13\}$	$\{i : i = 9,11,13,14,15\}$	$\{i : i = 5,6,7,8,9\}$

TABLE IX. MRT D2Q9 matrix $\mathbf{M}$.

$$\mathbf{M}_{\text{D2Q9}} = \begin{bmatrix} 1 & 1 & 1 & 1 & 1 & 1 & 1 & 1 & 1 \\ -4 & 2 & -1 & 2 & -1 & 2 & -1 & 2 & -1 \\ 4 & 1 & -2 & 1 & -2 & 1 & -2 & 1 & -2 \\ 0 & -1 & -1 & -1 & 0 & 1 & 1 & 1 & 0 \\ 0 & -1 & 2 & -1 & 0 & 1 & -2 & 1 & 0 \\ 0 & 1 & 0 & -1 & -1 & -1 & 0 & 1 & 1 \\ 0 & 1 & 0 & -1 & 2 & -1 & 0 & 1 & -2 \\ 0 & 0 & 1 & 0 & -1 & 0 & 1 & 0 & -1 \\ 0 & -1 & 0 & 1 & 0 & -1 & 0 & 1 & 0 \end{bmatrix}$$

TABLE X. MRT D3Q15 matrix $\mathbf{M}$.

$$\mathbf{M}_{\text{D3Q15}} = \begin{bmatrix} 1 & 1 & 1 & 1 & 1 & 1 & 1 & 1 & 1 & 1 & 1 & 1 & 1 & 1 & 1 \\ -2 & -1 & -1 & -1 & 1 & 1 & 1 & 1 & -1 & -1 & -1 & 1 & 1 & 1 & 1 \\ 16 & -4 & -4 & -4 & 1 & 1 & 1 & 1 & -4 & -4 & -4 & 1 & 1 & 1 & 1 \\ 0 & -1 & 0 & 0 & -1 & -1 & -1 & -1 & 1 & 0 & 0 & 1 & 1 & 1 & 1 \\ 0 & 4 & 0 & 0 & -1 & -1 & -1 & -1 & -4 & 0 & 0 & 1 & 1 & 1 & 1 \\ 0 & 0 & -1 & 0 & -1 & -1 & 1 & 1 & 0 & 1 & 0 & 1 & 1 & -1 & -1 \\ 0 & 0 & 4 & 0 & -1 & -1 & 1 & 1 & 0 & -4 & 0 & 1 & 1 & -1 & -1 \\ 0 & 0 & 0 & -1 & -1 & 1 & -1 & 1 & 0 & 0 & 1 & 1 & -1 & 1 & -1 \\ 0 & 0 & 0 & 4 & -1 & 1 & -1 & 1 & 0 & 0 & -4 & 1 & -1 & 1 & -1 \\ 0 & 2 & -1 & -1 & 0 & 0 & 0 & 0 & 2 & -1 & -1 & 0 & 0 & 0 & 0 \\ 0 & 0 & 1 & -1 & 0 & 0 & 0 & 0 & 0 & 1 & -1 & 0 & 0 & 0 & 0 \\ 0 & 0 & 0 & 0 & 1 & 1 & -1 & -1 & 0 & 0 & 0 & 1 & 1 & -1 & -1 \\ 0 & 0 & 0 & 0 & 1 & -1 & -1 & 1 & 0 & 0 & 0 & 1 & -1 & -1 & 1 \\ 0 & 0 & 0 & 0 & 1 & -1 & 1 & -1 & 0 & 0 & 0 & 1 & -1 & 1 & -1 \\ 0 & 0 & 0 & 0 & -1 & 1 & 1 & -1 & 0 & 0 & 0 & 1 & -1 & -1 & 1 \end{bmatrix}$$

TABLE XI. MRT D3Q19 matrix **M**.

$$\mathbf{M}_{\mathrm{D3Q19}} = \begin{bmatrix}
1 & 1 & 1 & 1 & 1 & 1 & 1 & 1 & 1 & 1 & 1 & 1 & 1 & 1 & 1 & 1 & 1 & 1 & 1 \\
-30 & -11 & -11 & -11 & 8 & 8 & 8 & 8 & 8 & 8 & -11 & -11 & -11 & 8 & 8 & 8 & 8 & 8 & 8 \\
12 & -4 & -4 & -4 & 1 & 1 & 1 & 1 & 1 & 1 & -4 & -4 & -4 & 1 & 1 & 1 & 1 & 1 & 1 \\
0 & -1 & 0 & 0 & -1 & -1 & -1 & -1 & 0 & 0 & 1 & 0 & 0 & 1 & 1 & 1 & 1 & 0 & 0 \\
0 & 4 & 0 & 0 & -1 & -1 & -1 & -1 & 0 & 0 & -4 & 0 & 0 & 1 & 1 & 1 & 1 & 0 & 0 \\
0 & 0 & -1 & 0 & -1 & 1 & 0 & 0 & -1 & -1 & 0 & 1 & 0 & 1 & -1 & 0 & 0 & 1 & 1 \\
0 & 0 & 4 & 0 & -1 & 1 & 0 & 0 & -1 & -1 & 0 & -4 & 0 & 1 & -1 & 0 & 0 & 1 & 1 \\
0 & 0 & 0 & -1 & 0 & 0 & -1 & 1 & -1 & 1 & 0 & 0 & 1 & 0 & 0 & 1 & -1 & 1 & -1 \\
0 & 0 & 0 & 4 & 0 & 0 & -1 & 1 & -1 & 1 & 0 & 0 & -4 & 0 & 0 & 1 & -1 & 1 & -1 \\
0 & 2 & -1 & -1 & 1 & 1 & 1 & 1 & -2 & -2 & 2 & -1 & -1 & 1 & 1 & 1 & 1 & -2 & -2 \\
0 & -4 & 2 & 2 & 1 & 1 & 1 & 1 & -2 & -2 & -4 & 2 & 2 & 1 & 1 & 1 & 1 & -2 & -2 \\
0 & 0 & 1 & -1 & 1 & 1 & -1 & -1 & 0 & 0 & 0 & 1 & -1 & 1 & 1 & -1 & -1 & 0 & 0 \\
0 & 0 & -2 & 2 & 1 & 1 & -1 & -1 & 0 & 0 & 0 & -2 & 2 & 1 & 1 & -1 & -1 & 0 & 0 \\
0 & 0 & 0 & 0 & 1 & -1 & 0 & 0 & 0 & 0 & 0 & 0 & 0 & 1 & -1 & 0 & 0 & 0 & 0 \\
0 & 0 & 0 & 0 & 0 & 0 & 0 & 0 & 1 & -1 & 0 & 0 & 0 & 0 & 0 & 0 & 0 & 1 & -1 \\
0 & 0 & 0 & 0 & 0 & 0 & 1 & -1 & 0 & 0 & 0 & 0 & 0 & 0 & 0 & 1 & -1 & 0 & 0 \\
0 & 0 & 0 & 0 & -1 & -1 & 1 & 1 & 0 & 0 & 0 & 0 & 0 & 1 & 1 & -1 & -1 & 0 & 0 \\
0 & 0 & 0 & 0 & 1 & -1 & 0 & 0 & -1 & -1 & 0 & 0 & 0 & -1 & 1 & 0 & 0 & 1 & 1 \\
0 & 0 & 0 & 0 & 0 & 0 & -1 & 1 & 1 & -1 & 0 & 0 & 0 & 0 & 0 & 1 & -1 & -1 & 1
\end{bmatrix}$$

TABLE XII. MRT D3Q27 matrix **M**.

$$\mathbf{M}_{\mathrm{D3Q27}} = \begin{bmatrix}
1 & 1 & 1 & 1 & 1 & 1 & 1 & 1 & 1 & 1 & 1 & 1 & 1 & 1 & 1 & 1 & 1 & 1 & 1 & 1 & 1 & 1 & 1 & 1 & 1 & 1 & 1 \\
0 & -1 & 0 & 0 & -1 & -1 & -1 & -1 & 0 & 0 & -1 & -1 & -1 & -1 & 1 & 0 & 0 & 1 & 1 & 1 & 1 & 0 & 0 & 1 & 1 & 1 & 1 \\
0 & 0 & -1 & 0 & -1 & 1 & 0 & 0 & -1 & -1 & -1 & -1 & 1 & 1 & 0 & 1 & 0 & 1 & -1 & 0 & 0 & 1 & 1 & 1 & 1 & -1 & -1 \\
0 & 0 & 0 & -1 & 0 & 0 & -1 & 1 & -1 & 1 & -1 & 1 & -1 & 1 & 0 & 0 & 1 & 0 & 0 & 1 & -1 & 1 & -1 & 1 & -1 & 1 & -1 \\
-2 & -1 & -1 & -1 & 0 & 0 & 0 & 0 & 0 & 0 & 1 & 1 & 1 & 1 & -1 & -1 & -1 & 0 & 0 & 0 & 0 & 0 & 0 & 1 & 1 & 1 & 1 \\
0 & 2 & -1 & -1 & 1 & 1 & 1 & 1 & -2 & -2 & 0 & 0 & 0 & 0 & 2 & -1 & -1 & 1 & 1 & 1 & 1 & -2 & -2 & 0 & 0 & 0 & 0 \\
0 & 0 & 1 & -1 & 1 & 1 & -1 & -1 & 0 & 0 & 0 & 0 & 0 & 0 & 0 & 1 & -1 & 1 & 1 & -1 & -1 & 0 & 0 & 0 & 0 & 0 & 0 \\
0 & 0 & 0 & 0 & 1 & -1 & 0 & 0 & 0 & 0 & 1 & 1 & -1 & -1 & 0 & 0 & 0 & 1 & -1 & 0 & 0 & 0 & 0 & 1 & 1 & -1 & -1 \\
0 & 0 & 0 & 0 & 0 & 0 & 0 & 0 & 1 & -1 & 1 & -1 & -1 & 1 & 0 & 0 & 0 & 0 & 0 & 0 & 0 & 1 & -1 & 1 & -1 & -1 & 1 \\
0 & 0 & 0 & 0 & 0 & 0 & 1 & -1 & 0 & 0 & 1 & -1 & 1 & -1 & 0 & 0 & 0 & 0 & 0 & 1 & -1 & 0 & 0 & 1 & -1 & 1 & -1 \\
0 & 4 & 0 & 0 & 1 & 1 & 1 & 1 & 0 & 0 & -2 & -2 & -2 & -2 & -4 & 0 & 0 & -1 & -1 & -1 & -1 & 0 & 0 & 2 & 2 & 2 & 2 \\
0 & 0 & 4 & 0 & 1 & -1 & 0 & 0 & 1 & 1 & -2 & -2 & 2 & 2 & 0 & -4 & 0 & -1 & 1 & 0 & 0 & -1 & -1 & 2 & 2 & -2 & -2 \\
0 & 0 & 0 & 4 & 0 & 0 & 1 & -1 & 1 & -1 & -2 & 2 & -2 & 2 & 0 & 0 & -4 & 0 & 0 & -1 & 1 & -1 & 1 & 2 & -2 & 2 & -2 \\
0 & -4 & 0 & 0 & 2 & 2 & 2 & 2 & 0 & 0 & -1 & -1 & -1 & -1 & 4 & 0 & 0 & -2 & -2 & -2 & -2 & 0 & 0 & 1 & 1 & 1 & 1 \\
0 & 0 & -4 & 0 & 2 & -2 & 0 & 0 & 2 & 2 & -1 & -1 & 1 & 1 & 0 & 4 & 0 & -2 & 2 & 0 & 0 & -2 & -2 & 1 & 1 & -1 & -1 \\
0 & 0 & 0 & -4 & 0 & 0 & 2 & -2 & 2 & -2 & -1 & 1 & -1 & 1 & 0 & 0 & 4 & 0 & 0 & -2 & 2 & -2 & 2 & 1 & -1 & 1 & -1 \\
4 & 0 & 0 & 0 & -1 & -1 & -1 & -1 & -1 & -1 & 1 & 1 & 1 & 1 & 0 & 0 & 0 & -1 & -1 & -1 & -1 & -1 & -1 & 1 & 1 & 1 & 1 \\
-8 & 4 & 4 & 4 & -2 & -2 & -2 & -2 & -2 & -2 & 1 & 1 & 1 & 1 & 4 & 4 & 4 & -2 & -2 & -2 & -2 & -2 & -2 & 1 & 1 & 1 & 1 \\
0 & -4 & 2 & 2 & 1 & 1 & 1 & 1 & -2 & -2 & 0 & 0 & 0 & 0 & -4 & 2 & 2 & 1 & 1 & 1 & 1 & -2 & -2 & 0 & 0 & 0 & 0 \\
0 & 0 & -2 & 2 & 1 & 1 & -1 & -1 & 0 & 0 & 0 & 0 & 0 & 0 & 0 & -2 & 2 & 1 & 1 & -1 & -1 & 0 & 0 & 0 & 0 & 0 & 0 \\
0 & 0 & 0 & 0 & -2 & 2 & 0 & 0 & 0 & 0 & 1 & 1 & -1 & -1 & 0 & 0 & 0 & -2 & 2 & 0 & 0 & 0 & 0 & 1 & 1 & -1 & -1 \\
0 & 0 & 0 & 0 & 0 & 0 & 0 & 0 & -2 & 2 & 1 & -1 & -1 & 1 & 0 & 0 & 0 & 0 & 0 & 0 & 0 & -2 & 2 & 1 & -1 & -1 & 1 \\
0 & 0 & 0 & 0 & 0 & 0 & -2 & 2 & 0 & 0 & 1 & -1 & 1 & -1 & 0 & 0 & 0 & 0 & 0 & -2 & 2 & 0 & 0 & 1 & -1 & 1 & -1 \\
0 & 0 & 0 & 0 & -1 & -1 & 1 & 1 & 0 & 0 & 0 & 0 & 0 & 0 & 0 & 0 & 0 & 1 & 1 & -1 & -1 & 0 & 0 & 0 & 0 & 0 & 0 \\
0 & 0 & 0 & 0 & 1 & -1 & 0 & 0 & -1 & -1 & 0 & 0 & 0 & 0 & 0 & 0 & 0 & -1 & 1 & 0 & 0 & 1 & 1 & 0 & 0 & 0 & 0 \\
0 & 0 & 0 & 0 & 0 & 0 & -1 & 1 & 1 & -1 & 0 & 0 & 0 & 0 & 0 & 0 & 0 & 0 & 0 & 1 & -1 & -1 & 1 & 0 & 0 & 0 & 0 \\
0 & 0 & 0 & 0 & 0 & 0 & 0 & 0 & 0 & 0 & -1 & 1 & 1 & -1 & 0 & 0 & 0 & 0 & 0 & 0 & 0 & 0 & 0 & 1 & -1 & -1 & 1
\end{bmatrix}$$

[1] R. E. Jackson, Recognizing emerging environmental problems: the case of chlorinated solvents in groundwater, Technol. Cult. **45**, 55 (2004).

[2] C. I. Steefel, S. Molins, and D. Trebotich, Pore scale processes associated with subsurface CO_2 injection and sequestration, Rev. Mineral. Geochem. **77**, 259 (2013).

[3] A. Muggeridge, A. Cockin, K. Webb, H. Frampton, I. Collins, T. Moulds, and P. Salino, Recovery rates, enhanced oil recovery and technological limits, Philos. Trans. R. Soc. London A **372**, 20120320 (2014).

[4] A. Parmigiani, C. Huber, and O. Bachmann, Mush microphysics and the reactivation of crystal-rich magma reservoirs, J. Geophys. Res.: Solid Earth **119**, 6308 (2014).

[5] A. Parmigiani, S. Faroughi, C. Huber, O. Bachmann, and Y. Su, Bubble accumulation and its role in the evolution of magma reservoirs in the upper crust, Nature (London) **532**, 492 (2016).

[6] S. S. Datta, J.-B. Dupin, and D. A. Weitz, Fluid breakup during simultaneous two-phase flow through a three-dimensional porous medium, Phys. Fluids **26**, 062004 (2014).

[7] M. Rücker, S. Berg, R. T. Armstrong, A. Georgiadis, H. Ott, A. Schwing, R. Neiteler, N. Brussee, A. Makurat, L. Leu, M. Wolf, F. Khan, F. Enzmann, and M. Kersten, From connected pathway flow to ganglion dynamics, Geophys. Res. Lett. **42**, 3888 (2015).

[8] T. Pak, I. B. Butler, S. Geiger, M. I. J. van Dijke, and K. S. Sorbie, Droplet fragmentation: 3D imaging of a previously unidentified pore-scale process during multiphase flow in porous media, Proc. Natl. Acad. Sci. USA **112**, 1947 (2015).

[9] T. Ramstad, N. Idowu, C. Nardi, and P.-E. Øren, Relative permeability calculations from two-phase flow simulations directly on digital images of porous rocks, Transp. Porous Media **94**, 487 (2012).

[10] A. Parmigiani, C. Huber, O. Bachmann, and B. Chopard, Pore-scale mass and reactant transport in multiphase porous media flows, J. Fluid Mech. **686**, 40 (2011).

[11] C. Huber, A. Parmigiani, J. Latt, and J. Dufek, Channelization of buoyant nonwetting fluids in saturated porous media, Water Resour. Res. **49**, 6371 (2013).

[12] A. Ferrari and I. Lunati, Direct numerical simulations of interface dynamics to link capillary pressure and total surface energy, Adv. Water Resour. **57**, 19 (2013).

[13] H. A. Akhlaghi Amiri and A. A. Hamouda, Evaluation of level set and phase field methods in modeling two phase flow with viscosity contrast through dual-permeability porous medium, Int. J. Multiphase Flow **52**, 22 (2013).

[14] H. Liu, A. J. Valocchi, Q. Kang, and C. Werth, Pore-scale simulations of gas displacing liquid in a homogeneous pore network using the lattice Boltzmann method, Transp. Porous Media **99**, 555 (2013).

[15] A. K. Gunstensen and D. H. Rothman, Microscopic modeling of immiscible fluids in three dimensions by a lattice Boltzmann method, Europhys. Lett. **18**, 157 (1992).

[16] X. Shan and H. Chen, Lattice Boltzmann model for simulating flows with multiple phases and components, Phys. Rev. E **47**, 1815 (1993).

[17] M. R. Swift, E. Orlandini, W. R. Osborn, and J. M. Yeomans, Lattice Boltzmann simulations of liquid-gas and binary fluid systems, Phys. Rev. E **54**, 5041 (1996).

[18] H. Huang, M. Sukop, and X. Lu, *Multiphase Lattice Boltzmann Methods: Theory and Application* (Wiley-Blackwell, Oxford, 2015).

[19] H. Liu, Q. Kang, C. R. Leonardi, S. Schmieschek, A. Narváez, B. D. Jones, J. R. Williams, A. J. Valocchi, and J. Harting, Multiphase lattice boltzmann simulations for porous media applications, Comput. Geosci. **20**, 777 (2016).

[20] J. Yang and E. S. Boek, A comparison study of multi-component Lattice Boltzmann models for flow in porous media applications, Comput. Math. Appl. **65**, 882 (2013).

[21] H. Huang, L. Wang, and X.-y. Lu, Evaluation of three lattice Boltzmann models for multiphase flows in porous media, Comput. Math. Appl. **61**, 3606 (2011).

[22] S. Hou, X. Shan, Q. Zou, G. D. Doolen, and W. E. Soll, Evaluation of two lattice Boltzmann models for multiphase flows, J. Comput. Phys. **138**, 695 (1997).

[23] S. Succi, *The Lattice Boltzmann Equation: For Fluid Dynamics and Beyond* (Clarendon, Oxford, 2001).

[24] M. C. Sukop and D. T. Thorne, *Lattice Boltzmann Modeling: An Introduction for Geoscientists and Engineers*, 1st ed. (Springer-Verlag, Berlin, 2006).

[25] A. A. Mohamad, *Lattice Boltzmann Method: Fundamentals and Engineering Applications with Computer Codes* (Springer-Verlag, London, 2011).

[26] S. Succi, E. Foti, and F. Higuera, Three-dimensional flows in complex geometries with the lattice Boltzmann method, Europhys. Lett. **10**, 433 (1989).

[27] A. Cancelliere, C. Chang, E. Foti, D. H. Rothman, and S. Succi, The permeability of a random medium: Comparison of simulation with theory, Phys. Fluids A **2**, 2085 (1990).

[28] C. Pan, M. Hilpert, and C. T. Miller, Lattice-Boltzmann simulation of two-phase flow in porous media, Water Resour. Res. **40**, W01501 (2004).

[29] M. L. Porter, M. G. Schaap, and D. Wildenschild, Lattice-Boltzmann simulations of the capillary pressure-saturation-interfacial area relationship for porous media, Adv. Water Resour. **32**, 1632 (2009).

[30] M. L. Porter, E. T. Coon, Q. Kang, J. D. Moulton, and J. W. Carey, Multicomponent interparticle-potential lattice Boltzmann model for fluids with large viscosity ratios, Phys. Rev. E **86**, 036701 (2012).

[31] L. Chen, Q. Kang, Y. Mu, Y.-L. He, and W.-Q. Tao, A critical review of the pseudopotential multiphase lattice Boltzmann model: Methods and applications, Int. J. Heat Mass Transf. **76**, 210 (2014).

[32] A. Montessori, G. Falcucci, M. La Rocca, S. Ansumali, and S. Succi, Three-dimensional lattice pseudo-potentials for multiphase flow simulations at high density ratios, J. Stat. Phys. **161**, 1404 (2015).

[33] D. Lycett-Brown and K. H. Luo, Cascaded lattice Boltzmann method with improved forcing scheme for large-density-ratio multiphase flow at high reynolds and weber numbers, Phys. Rev. E **94**, 053313 (2016).

[34] J. Tölke, M. Krafczyk, M. Schulz, and E. Rank, Lattice Boltzmann simulations of binary fluid flow through porous media, Philos. Trans. R. Soc. London A **360**, 535 (2002).

[35] H. Liu, A. J. Valocchi, and Q. Kang, Three-dimensional lattice Boltzmann model for immiscible two-phase flow simulations, Phys. Rev. E **85**, 046309 (2012).

[36] X. Li, Y. Zhang, X. Wang, and W. Ge, GPU-based numerical simulation of multi-phase flow in porous media using multiple-relaxation-time lattice Boltzmann method, Chem. Eng. Sci. **102**, 209 (2013).

[37] D. J. Holdych, D. Rovas, J. G. Georgiadis, and R. O. Buckius, An improved hydrodynamics formulation for multiphase flow lattice-Boltzmann models, Int. J. Mod. Phys. C **09**, 1393 (1998).

[38] G. K. Batchelor, *An Introduction to Fluid Dynamics*, Cambridge Mathematical Library Series (Cambridge University Press, Cambridge, England, 1967).

[39] S. Leclaire, N. Pellerin, M. Reggio, and J.-Y. Trépanier, Enhanced equilibrium distribution functions for simulating immiscible multiphase flows with variable density ratios in a class of lattice Boltzmann models, Int. J. Multiphase Flow **57**, 159 (2013).

[40] D. Lycett-Brown, K. H. Luo, R. Liu, and P. Lv, Binary droplet collision simulations by a multiphase cascaded lattice Boltzmann method, Phys. Fluids **26**, 023303 (2014).

[41] S. Leclaire, N. Pellerin, M. Reggio, and J.-Y. Trépanier, A multiphase lattice Boltzmann method for simulating immiscible liquid-liquid interface dynamics, Appl. Math. Modell. **40**, 6376 (2016).

[42] S. Leclaire, N. Pellerin, M. Reggio, and J.-Y. Trépanier, Unsteady immiscible multiphase flow validation of a multiple-relaxation-time lattice Boltzmann method, J. Phys. A **47**, 105501 (2014).

[43] T. Reis and T. N. Phillips, Lattice Boltzmann model for simulating immiscible two-phase flows, J. Phys. A **40**, 4033 (2007).

[44] S. Leclaire, K. Abahri, R. Belarbi, and R. Bennacer, Modeling of static contact angles with curved boundaries using a multiphase lattice Boltzmann method with variable density and viscosity ratios, Int. J. Numer. Methods Fluids **82**, 451 (2016).

[45] T. J. Spencer and I. Halliday, Multicomponent lattice boltzmann equation method with a discontinuous hydrodynamic interface, Phys. Rev. E **88**, 063305 (2013).

[46] K. N. Premnath and J. Abraham, Three-dimensional multi-relaxation time (MRT) lattice-Boltzmann models for multiphase flow, J. Comput. Phys. **224**, 539 (2007).

[47] Y. Ba, H. Liu, Q. Li, Q. Kang, and J. Sun, Multiple-relaxation-time color-gradient lattice boltzmann model for simulating two-phase flows with high density ratio, Phys. Rev. E **94**, 023310 (2016).

[48] S. Lishchuk, C. Care, and I. Halliday, Lattice Boltzmann algorithm for surface tension with greatly reduced microcurrents, Phys. Rev. E **67**, 036701 (2003).

[49] H. Huang, J.-J. Huang, X.-Y. Lu, and M. C. Sukop, On simulations of high-density ratio flows using color-gradient multiphase lattice Boltzmann models, Int. J. Mod. Phys. C **24**, 1350021 (2013).

[50] A. Gunde, T. Babadagli, S. Sinha Roy, and S. Kumar Mitra, Pore-scale interfacial dynamics and oil-water relative permeabilities of capillary driven counter-current flow in fractured porous media, J. Pet. Sci. Eng. **103**, 106 (2013).

[51] A. K. Gunstensen, D. H. Rothman, S. Zaleski, and G. Zanetti, Lattice Boltzmann model of immiscible fluids, Phys. Rev. A **43**, 4320 (1991).

[52] M. Latva-Kokko and D. H. Rothman, Diffusion properties of gradient-based lattice Boltzmann models of immiscible fluids, Phys. Rev. E **71**, 056702 (2005).

[53] S. Leclaire, M. Reggio, and J.-Y. Trépanier, Isotropic color gradient for simulating very high-density ratios with a two-phase flow lattice Boltzmann model, Comput. Fluids **48**, 98 (2011).

[54] H. Huang, J.-J. Huang, and X.-Y. Lu, Study of immiscible displacements in porous media using a color-gradient-based multiphase lattice Boltzmann method, Comput. Fluids **93**, 164 (2014).

[55] R. Lenormand, E. Touboul, and C. Zarcone, Numerical models and experiments on immiscible displacements in porous media, J. Fluid Mech. **189**, 165 (1988).

[56] F. Jiang, T. Tsuji, and C. Hu, Elucidating the role of interfacial tension for hydrological properties of two-phase flow in natural sandstone by an improved lattice Boltzmann method, Transp. Porous Media **104**, 205 (2014).

[57] G. Rastiello, S. Leclaire, R. Belarbi, and R. Bennacer, Unstable two-phase flow rate in micro-channels and cracks under imposed pressure difference, Int. J. Multiphase Flow **77**, 131 (2015).

[58] H. Liu, A. J. Valocchi, C. Werth, Q. Kang, and M. Oostrom, Pore-scale simulation of liquid CO_2 displacement of water using a two-phase lattice Boltzmann model, Adv. Water Resour. **73**, 144 (2014).

[59] H. Liu, Y. Zhang, and A. J. Valocchi, Lattice Boltzmann simulation of immiscible fluid displacement in porous media: Homogeneous versus heterogeneous pore network, Phys. Fluids **27**, 052103 (2015).

[60] T. Tsuji, F. Jiang, and K. T. Christensen, Characterization of immiscible fluid displacement processes with various capillary numbers and viscosity ratios in 3D natural sandstone, Adv. Water Resour. **95**, 3 (2016).

[61] J. Tölke, S. Freudiger, and M. Krafczyk, An adaptive scheme using hierarchical grids for lattice Boltzmann multi-phase flow simulations, Comput. Fluids **35**, 820 (2006).

[62] S. Leclaire, M. Reggio, and J.-Y. Trépanier, Progress and investigation on lattice Boltzmann modeling of multiple immiscible fluids or components with variable density and viscosity ratios, J. Comput. Phys. **246**, 318 (2013).

[63] G. S. Barozzi and D. Angeli, A note on capillary rise in tubes, Energy Procedia **45**, 548 (2014).

[64] J. W. Bullard and E. J. Garboczi, Capillary rise between planar surfaces, Phys. Rev. E **79**, 011604 (2009).

[65] E. W. Washburn, The dynamics of capillary flow, Phys. Rev. **17**, 273 (1921).

[66] K. Uno Ingard, *Fundamentals of Waves and Oscillations* (Cambridge University Press, Cambridge, England, 1988), Vol. 57.

[67] J. Latt, B. Chopard, O. Malaspinas, M. Deville, and A. Michler, Straight velocity boundaries in the lattice Boltzmann method, Phys. Rev. E **77**, 056703 (2008).

[68] www.palabos.org (2016).

[69] J. Lätt, Hydrodynamic limit of lattice Boltzmann equations, Ph.D. thesis, University of Geneva, 2007.

[70] B. Chopard, A. Dupuis, A. Masselot, and P. Luthi, Cellular automata and lattice Boltzmann techniques: an approach to model and simulate complex systems, Adv. Complex Syst. **05**, 103 (2002).

[71] D. D'Humières, Generalized lattice Boltzmann equations, In Rarefied gas dynamics: theory and simulations, Prog. Astronaut. Aeronaut. **159**, 450 (1992).

[72] D. Grunau, S. Chen, and K. Eggert, A lattice Boltzmann model for multiphase fluid flows, Phys. Fluids A **5**, 2557 (1993).

[73] D. D'Humières, I. Ginzburg, M. Krafczyk, P. Lallemand, and L. S. Luo, Multiple-relaxation-time lattice Boltzmann models in three dimensions, Philos. Trans. A **360**, 437 (2002).
[74] F. Dubois and P. Lallemand, Quartic parameters for acoustic applications of lattice Boltzmann scheme, Comput. Math. Appl. **61**, 3404 (2011).
[75] K. Suga, Y. Kuwata, K. Takashima, and R. Chikasue, A D3Q27 multiple-relaxation-time lattice Boltzmann method for turbulent flows, Comput. Math. Appl. **69**, 518 (2015).
[76] S. Leclaire, M. Reggio, and J.-Y. Trépanier, Numerical evaluation of two recoloring operators for an immiscible two-phase flow lattice Boltzmann model, Appl. Math. Modell. **36**, 2237 (2012).
[77] S. Leclaire, N. Pellerin, M. Reggio, and J.-Y. Trépanier, An approach to control the spurious currents in a multiphase lattice Boltzmann method and to improve the implementation of initial condition, Int. J. Numer. Methods Fluids **77**, 732 (2015).
[78] R. R. R. Nourgaliev, T. N. N. Dinh, T. G. G. Theofanous, and D. Joseph, The lattice Boltzmann equation method: theoretical interpretation, numerics and implications, Int. J. Multiphase Flow **29**, 117 (2003).
[79] M. Bouzidi, M. Firdaouss, and P. Lallemand, Momentum transfer of a Boltzmann-lattice fluid with boundaries, Phys. Fluids **13**, 3452 (2001).
[80] Z. Guo and C. Zheng, An extrapolation method for boundary conditions in lattice Boltzmann method, Phys. Fluids **14**, 2007 (2002).
[81] I. Ginzburg and D. d'Humières, Multireflection boundary conditions for lattice Boltzmann models, Phys. Rev. E **68**, 066614 (2003).
[82] O. Malaspinas, B. Chopard, and J. Latt, General regularized boundary condition for multi-speed lattice Boltzmann models, Comput. Fluids **49**, 29 (2011).
[83] Q. Zou and X. He, On pressure and velocity boundary conditions for the lattice Boltzmann BGK model, Phys. Fluids **9**, 1591 (1997).
[84] J. Tölke, G. De Prisco, and Y. Mu, A lattice Boltzmann method for immiscible two-phase Stokes flow with a local collision operator, Comput. Math. Appl. **65**, 864 (2013).
[85] H. Dong, Micro-Ct imaging and pore network extraction, Ph.D. thesis, Imperial College London, 2007.
[86] D. Carl Ipsen, *Units, Dimensions, and Dimensionless Numbers* (McGraw-Hill, New York, 1960.
[87] F. M. White, *Fluid Mechanics*, 7th ed. (McGraw-Hill, New York, 2011.
[88] S. Leclaire, M. El-Hachem, J.-Y. Trépanier, and M. Reggio, High order spatial generalization of 2D and 3D isotropic discrete gradient operators with fast evaluation on GPUs, J. Sci. Comput. **59**, 545 (2014).
[89] B. Fornberg, Generation of finite difference formulas on arbitrarily spaced grids, Math. Comput. **51**, 699 (1988).
[90] www.paraview.org (2016).
[91] C. Pan, L.-S. Luo, and C. T. Miller, An evaluation of lattice Boltzmann schemes for porous medium flow simulation, Comput. Fluids **35**, 898 (2006).
[92] P. Prestininzi, A. Montessori, M. La Rocca, and S. Succi, Reassessing the single relaxation time Lattice Boltzmann method for the simulation of Darcy's flows, Int. J. Mod. Phys. C **27**, 1650037 (2016).
[93] J. W. Weaver and S. G. Huling, Dense nonaqueous phase liquids, technical report, Superfund Technology Support Center for Ground Water, Oklahoma, 1991.
[94] See Supplemental Material at http://link.aps.org/supplemental/10.1103/PhysRevE.95.033306 for animations.
[95] Berea sandstone data, 2016.
[96] J. P. Stokes, D. A. Weitz, J. P. Gollub, A. Dougherty, M. O. Robbins, P. M. Chaikin, and H. M. Lindsay, Interfacial Stability of Immiscible Displacement in a Porous Medium, Phys. Rev. Lett. **57**, 1718 (1986).
[97] M. Trojer, M. L. Szulczewski, and R. Juanes, Stabilizing Fluid-Fluid Displacements in Porous Media through Wettability Alteration, Phys. Rev. Appl. **3**, 054008 (2015).
[98] R. Holtzman and E. Segre, Wettability Stabilizes Fluid Invasion into Porous Media via Nonlocal, Cooperative Pore Filling, Phys. Rev. Lett. **115**, 164501 (2015).
[99] K. Tore Tallakstad, H. Arendt Knudsen, T. Ramstad, G. Løvoll, K. Jørgen Måløy, R. Toussaint, and E. Grude Flekkøy, Steady-State Two-Phase Flow in Porous Media: Statistics and Transport Properties, Phys. Rev. Lett. **102**, 074502 (2009).
[100] B. H. Kueper and D. B. McWhorter, The behavior of dense, nonaqueous phase liquids in fractured clay and rock, Ground Water **29**, 716 (1991).
[101] P. Burt and E. Adelson, The Laplacian pyramid as a compact image code, IEEE Trans. Commun. **31**, 532 (1983).
[102] M. Sbragaglia, L. Biferale, G. Amati, S. Varagnolo, D. Ferraro, G. Mistura, and M. Pierno, Sliding drops across alternating hydrophobic and hydrophilic stripes, Phys. Rev. E **89**, 012406 (2014).
[103] A. W. Woods, *Flow in Porous Rocks: Energy and Environmental Applications* (Cambridge University Press, Cambridge, England, 2015).